**RDECOM**

**TECHNICAL REPORT CR-AMR-AF-07-01**

# A CFD Study of the Aerodynamics of a 6x6x8 Foot Cargo Container Suspended Beneath a Helicopter
## Part I:  Aerodynamics of the Stationary Container

**Johannes N. Theron and Earl P.N. Duque**
Northern Arizona University
Mechanical Engineering Department
P. O. Box 15600
Flagstaff, AZ  86011

and

**Luigi Cicolani**
San Jose State University Foundation
Mail Stop 262-11
Ames Research Center
Moffett Field, CA  94035

## DESTRUCTION NOTICE

## DISCLAIMER

## TRADE NAMES

| REPORT DOCUMENTATION PAGE | | Form Approved OMB No. 074-0188 |
|---|---|---|

Public reporting burden for this collection of information is estimated to average 1 hour per response, including the time for reviewing instructions, searching existing data sources, gathering and maintaining the data needed, and completing and reviewing this collection of information. Send comments regarding this burden estimate or any other aspect of this collection of information, including suggestions for reducing this burden to Washington Headquarters Services, Directorate for Information Operations and Reports, 1215 Jefferson Davis Highway, Suite 1204, Arlington, VA 22202-4302, and to the Office of Management and Budget, Paperwork Reduction Project (0704-0188), Washington, DC 20503

| 1. AGENCY USE ONLY | 2. REPORT DATE October 2007 | 3. REPORT TYPE AND DATES COVERED Final – Contractor Report |
|---|---|---|

| 4. TITLE AND SUBTITLE | 5. FUNDING NUMBERS |
|---|---|
| A CFD Study of the Aerodynamics of a 6x6x8 Foot Cargo Container Suspended Beneath a Helicopter<br>Part I: Aerodynamics of the Stationary Container | NNA05CS80A (NASA Ames) |

**6. AUTHOR(S)**

Johannes N. Theron, Luigi Cicolani, Earl P. N. Duque

| 7. PERFORMING ORGANIZATION NAME(S) AND ADDRESS(ES) | 8. PERFORMING ORGANIZATION REPORT NUMBER |
|---|---|
| Northern Arizona University,     San Jose University Foundation<br>Mechanical Engineering Department    Mail Stop 262-11<br>P. O. Box 15600                Ames Research Center<br>Flagstaff, AZ 86011          Moffett, CA 94035 | TR-CR-AMR-AF-07-01 |

| 9. SPONSORING / MONITORING AGENCY NAME(S) AND ADDRESS(ES) | 10. SPONSORING / MONITORING AGENCY REPORT NUMBER |
|---|---|
| Commander, U.S. Army Research, Development, and<br>   Engineering Command<br>ATTN: AMSRD-AMR-AF<br>Redstone Arsenal, AL 35898 | |

**11. SUPPLEMENTARY NOTES**

| 12a. DISTRIBUTION / AVAILABILITY STATEMENT | 12b. DISTRIBUTION CODE |
|---|---|
| Approved for public release; distribution is unlimited. | A |

**13. ABSTRACT** *(Maximum 200 Words)*

    This report is the first of several on a study of the unsteady aerodynamics of the CONEX cargo container. This work is in support of an effort to develop a model of the CONEX unsteady aerodynamics for use in simulations of helicopter-slung-load dynamics. It is known from the literature on cargo container aerodynamics that instability is caused by unsteady flow effects such as vortex shedding and flow structure lags and cannot be predicted by simple models that utilize only the static and quasi-static aerodynamics of the container.

    This report describes the first phase of the work to develop the CFD computational setup, validate it against the available wind tunnel data for the stationary CONEX, and provide some material on flow structure around the stationary CONEX. Results are given for both steady flow and unsteady flow CFD simulations. The Reynolds-averaged Navier-Stokes code known as OVERFLOW developed by NASA was used for this work.

| 14. SUBJECT TERMS | 15. NUMBER OF PAGES |
|---|---|
| Cargo container aerodynamics, unsteady flow, computational fluid dynamics overflow | 79 |
| | 16. PRICE CODE |

| 17. SECURITY CLASSIFICATION OF REPORT | 18. SECURITY CLASSIFICATION OF THIS PAGE | 19. SECURITY CLASSIFICATION OF ABSTRACT | 20. LIMITATION OF ABSTRACT |
|---|---|---|---|
| UNCLASSIFIED | UNCLASSIFIED | UNCLASSIFIED | SAR |

NSN 7540-01-280-5500

**Standard Form 298 (Rev. 2-89)**
Prescribed by ANSI Std. Z39-18
298-102

# A CFD STUDY OF THE AERODYNAMICS OF A 6X6X8 FT CARGO CONTAINER SUSPENDED BENEATH A HELICOPTER

## Part I: Aerodynamics of the Stationary Container

Johannes N. Theron[A], Luigi Cicolani[B], and Earl P.N. Duque[A]

**Aeroflight Dynamics Directorate**
**Aviation and Missile Research, Development & Engineering Center**

□ □ □ □ □ □ □ □ **2007**

A:  Mechanical Engineering Department, Northern Arizona University, P.O. Box 15600, Flagstaff, Az 86011
  B.  Flight Control and Cockpit Integration Division, Army Aeroflightdynamics Directorate,
     Mail Stop T12B, Ames Research Center, Moffett Fd., Ca, 94035

# REPORT DOCUMENTATION PAGE

Public reporting burden for this collection of information is estimated to average 1 hour per response, including the time for reviewing instructions, searching existing data sources, gathering and maintaining the data needed, and completing and reviewing this collection of information. Send comments regarding this burden estimate or any other aspect of this collection of information, including suggestions for reducing this burden to Washington Headquarters Services, Directorate for Information Operations and Reports, 1215 Jefferson Davis Highway, Suite 1204, Arlington, VA 22202-4302, and to the Office of Management and Budget, Paperwork Reduction Project (0704-0188), Washington, DC 20503

| 1. AGENCY USE ONLY | 2. REPORT DATE | 3. REPORT TYPE AND DATES COVERED |
|---|---|---|
| | October 2007 | Final – Contractor Report |

**4. TITLE AND SUBTITLE**

A CFD Study of the Aerodynamics of a 6x6x8 Foot Cargo Container
Suspended Beneath a Helicopter

Part I: Aerodynamics of the Stationary Container

**5. FUNDING NUMBERS**

NNA05CS80A (NASA Ames)

6. AUTHOR(S)

Johannes N. Theron, Luigi Cicolani, Earl P. N. Duque

**7. PERFORMING ORGANIZATION NAME(S) AND ADDRESS(ES)**

Northern Arizona University,           San Jose University Foundation
Mechanical Engineering Department      Mail Stop 262-11
P. O. Box 15600                        Ames Research Center
Flagstaff, AZ 86011                    Moffett, CA 94035

**8. PERFORMING ORGANIZATION**

TR-CR-AMR-AF-07-01

**9. SPONSORING / MONITORING AGENCY NAME(S) AND ADDRESS(ES)**

Commander, U.S. Army Research, Development, and
    Engineering Command
ATTN: AMSRD-AMR-AF
Redstone Arsenal, AL 35898

**10. SPONSORING / MONITORING**

**11. SUPPLEMENTARY NOTES**

**12a. DISTRIBUTION / AVAILABILITY STATEMENT**

Approved for public release; distribution is unlimited.

**12b. DISTRIBUTION CODE**

A

**13. ABSTRACT** *(Maximum 200 Words)*

This report is the first of several on a study of the unsteady aerodynamics of the CONEX cargo container. This work is in support of an effort to develop a model of the CONEX unsteady aerodynamics for use in simulations of helicopter-slung-load dynamics. It is known from the literature on cargo container aerodynamics that instability is caused by unsteady flow effects such as vortex shedding and flow structure lags and cannot be predicted by simple models that utilize only the static and quasi-static aerodynamics of the container.

This report describes the first phase of the work to develop the CFD computational setup, validate it against the available wind tunnel data for the stationary CONEX, and provide some material on flow structure around the stationary CONEX. Results are given for both steady flow and unsteady flow CFD simulations. The Reynolds-averaged Navier-Stokes code known as OVERFLOW developed by NASA was used for this work.

**14. SUBJECT TERMS**

Cargo container aerodynamics, unsteady flow, computational fluid dynamics overflow

**15. NUMBER OF PAGES**

79

**16. PRICE CODE**

| 17. SECURITY CLASSIFICATION OF REPORT | 18. SECURITY CLASSIFICATION OF THIS PAGE | 19. SECURITY CLASSIFICATION OF ABSTRACT | 20. LIMITATION OF ABSTRACT |
|---|---|---|---|
| UNCLASSIFIED | UNCLASSIFIED | UNCLASSIFIED | SAR |

# ABSTRACT

This report is the first of several on a study of the unsteady aerodynamics of the CONEX cargo container. This work is in support of an effort to develop a model of the CONEX unsteady aerodynamics for use in simulations of helicopter-slung-load dynamics. It is known from the literature on cargo container aerodynamics that instability is caused by unsteady flow effects such as vortex shedding and flow structure lags and cannot be predicted by simple models that utilize only the static and quasi-static aerodynamics of the container.

With these factors in mind and also considering that there are no theoretical models of the unsteady aerodynamics, the present work was commissioned to study the unsteady aerodynamics of the CONEX cargo container with advanced computational fluid dynamics (CFD) software. This report describes the first phase of the work to develop the CFD computational setup, validate it against the available wind tunnel data for the stationary CONEX, and provide some material on flow structure around the stationary CONEX. Results are given for both steady flow and unsteady flow CFD simulations. The Reynolds-averaged Navier-Stokes code known as OVERFLOW developed by NASA was used for this work.

Future reports will present CFD results for the moving CONEX covering (1) validation of the CFD code against flight data for the moving, spinning CONEX, (2) a study of the aerodynamics of the CONEX at various fixed spin rates, and (3) results from forced oscillation computations in which frequency varies smoothly over the range of interest. The wind tunnel data was generated at the Technion Israel Institute of Technology and flight tests using a Sikorsky UH-60 Black Hawk and CONEX with several ballast weights were conducted by the Army's Aeroflightdynamics Directorate (AFDD) at Moffett Field, Ca. This work is part of a larger study of slung load dynamics conducted under the US Army-Israel Memorandum of Agreement for cooperative research on Rotorcraft Aeromechanics and Man-Machine Integration Technology.

# TABLE OF CONTENTS

## LIST OF ILLUSTRATIONS

# LIST OF TABLES

# LIST OF SYMBOLS

| Symbol | Description | Units |
|---|---|---|
| A | Reference area | $\text{ft}^2$ |
| $a_\infty$ | Freestream speed of sound | ft/s |
| $C_D$ | Drag force coefficient | |
| $C_L$ | Lift force coefficient | |
| $C_Y$ | Side force coefficient | |
| $C_m$ | Pitching moment coefficient | |
| $C_n$ | Yaw moment coefficient | |
| $C_l$ | Rolling moment coefficient | |
| $C_p$ | Pressure coefficient | |
| $f_x$ | Body force along the x axis | lbf |
| $f_y$ | Body force along the y axis | lbf |
| $f_z$ | Body force along the z axis | lbf |
| F, G, H | Flux terms in the Navier-Stokes equation | |
| g | Gravitational constant | |
| $I_{xx}, I_{yy}, I_{zz}$ | Moment of inertia | $\text{ft-lbs-s}^2$ |
| L | Reference length | ft |
| M | Mach number | |
| p | Pressure | $\text{lb}_f/\text{ft}^2$ |
| q | Body heating flux | $\text{ft-lb}_f/\text{s}$ |
| U | Velocity | ft/s |
| u | Velocity component in the body x direction | ft/s |
| v | Velocity component in the body y direction | ft/s |
| w | Velocity component in the body z direction | ft/s |

# GREEK SYMBOLS

| Symbol | Description | Units |
|---|---|---|
| $\alpha$ | Angle of attack | deg |
| $\beta$ | Side slip angle | deg |
| $\nu$ | viscosity | $\text{ft}^2/\text{s}$ |
| $\rho$ | Fluid density | $\text{lb/ft}^3$ |
| $\tau$ | Shear stress | $\text{lb/ft}^2$ |
| $\rho$ | Fluid density | $\text{slug/ft}^3$ |

Notes:
1. $\alpha$, $\beta$ in this text are identical to the customary pitch and (negative) yaw angles in the wind tunnel and CFD literature.
2. The aerodynamics are given as force and moment divided by dynamic pressure herein (units are $ft^2$, $ft^3$, respectively) and written as the coefficient times area, A, or volume, AL, respectively., e.g., $C_DA$, $C_nAL$, etc.

## LIST OF ABBREVIATIONS

| | |
|---|---|
| AFDD | Aeroflightdynamics Directorate |
| BC | Boundary Conditions |
| aoa | Angle of attack |
| CFD | Computational Fluid Dynamics |
| CONEX | Container Express |
| CPU | Central Processing Unit |
| DES | Detached Eddy Simulation |
| DES-SA | Detached Eddy Simulation - Spalart-Allmaras (turbulence model) |
| DES-SST | Detached Eddy Simulation - SST turbulence model |
| DNS | Direct Numerical Simulation |
| FFT | Fast Fourier Transform |
| GB | Gigabyte |
| GHz | Gigahertz ($10^9$ Hz) |
| HPC | High Performance Computer |
| Hz | Hertz (cycles per second) |
| kw-SST | kw Shear-Stress Transport (turbulence model) |
| LES | Large Eddy Simulation |
| LHS | Left hand side of the Navier-Stokes equation |
| MB | Megabyte |
| MPI | Message-Passing Interface |
| NASA | National Aeronautics and Space Administration |
| NAU | Northern Arizona University |
| NUMA | Nonuniform Memory Access |
| RAM | Random Access Memory |
| RANS | Reynolds-Averaged Navier-Stokes |
| RHS | Right hand side of the Navier-Stokes equation |
| SA | Spalart-Allmaras (turbulence model) |
| SMP | Shared Memory Protocol |
| stdv | standard deviation |
| WT | Wind Tunnel |

# 1.BACKGROUND AND INTRODUCTION

Rotorcraft operations often require the transportation of bulky payloads by suspending them underneath the aircraft. Figure Figure 1. UH-60 Helicopter and CONEX in Slung Load Configuration shows a Sikorsky UH-60 (Black Hawk) helicopter carrying a Container Express (CONEX) cargo container in a typical slung load configuration. These types of slung loads can, however, adversely affect the aircraft's flying qualities [Ref. 1]. In addition, cargo containers and other types of difficult loads become aerodynamically unstable at speeds well below the power-limited speed of the helicopter-load configuration. For example, the empty CONEX (2,000 lb) / UH-60 slung load configuration is power limited to 120 knots but is stability limited at only 60 knots. If the unsteady aerodynamic effects that are the cause of the instability of this slung load at high speed can be minimized, the safe flight envelope of this helicopter / load combination can be extended in this case, to the power limit of 120 knots.



*Figure 1. UH-60 Helicopter and CONEX in Slung Load Configuration*

While this would be an ideal situation, in reality the power-limited speed would be very difficult to achieve due to factors such as load drag which increases the load trail angle with airspeed to a safety limit even if the load is stable. The goal of this program is first, to understand the unsteady aerodynamic effects on the CONEX by computational means, and second to use this computational tool to predict the onset of instability of other helicopter slung loads.

Efforts have been underway with the U.S. Army Aeroflightdynamics Directorate (AFDD) at Moffett Field, Northern Arizona University, and the Technion Israel Institute of Technology (Haifa) to gain a better understanding of and generate simulation models capable of predicting the critical unstable speeds for such loads [Ref. 2, 3, 4, and 5]. These efforts consist of flight tests, wind tunnel tests, flight simulation, theoretical and computational studies.

This report summarizes that part of the collaborative efforts that validated a U. S. Government computational fluid dynamics (CFD) code against wind tunnel data for the stationary CONEX collected at the Technion [Ref. 6].

Data is presented for three grids; two representing the CONEX as a simple box (no skids, corrugations or other details) and the third representing the skids and limited surface details.

CFD studies were done in steady-state mode as well as unsteady (time-accurate) mode using Detached Eddy Simulation (DES). In all cases the CONEX was stationary over the course of a given CFD simulation. Due to the symmetry of the CONEX, forces and moments were calculated for angles of attack between -90 deg and +90 deg (at zero side slip angle) and for side slip angles between -180 deg and +180 deg (at zero angle of attack). (Note: angle of attack and side slip angle are the usual direction angles of the velocity vector in model body axes; these are respectively equivalent to pitch and (negative) yaw angles commonly used in CFD and tunnelwork.) Background information concerning unsteady aerodynamics as it relates to bluff-body flow, physical details of the full-scale CONEX, detailed information on the grids used to represent the CONEX, the CFD solver and the solver settings that were used, as well as benchmark data on a number of computational clusters are also presented.

## 1.1 Bluff Body Aerodynamics

The aerodynamic properties of lifting surfaces such as aircraft wings and propellers are well understood and over the last number of decades these devices have been the subject of a large number of wind-tunnel and computational studies. The flow over conventional lifting surfaces is characterized by (mostly) turbulent, attached boundary layers with small regions of separated flow. Two exceptions to this may be shock-induced separation on transonic airfoils and retreating-side stall typical of helicopter rotors. Yet, even these two examples of separated flow have been accounted for in computational codes and have been measured in wind tunnels so that the aircraft / helicopter designer has a suite of numerical tools available to compensate for the lack of theoretical models of these phenomena. The result is that the majority of flows over lifting surfaces are now routinely measured and predicted with sufficient accuracy to design safe and economical aircraft.

In contrast to attached-flow applications where drag is dominated by skin (viscous) drag, bluff-body aerodynamics are typically characterized by extended regions of massive flow separation and drag consists mostly of form (pressure) drag. This poses a computational challenge in that the region of interest to the CFD practitioner shifts away from the body and extends past the boundary layer and into the turbulent, chaotic wake. The normal procedure of modeling the freestream away from the body as inviscid flow may in this case be unable to capture the complex flow phenomena that influence the pressure distribution over the body and hence exhibit large deviations from measured data. Advanced turbulence models such as Detached-Eddy Simulation (DES) and Large Eddy Simulations (LES) may be required to provide better estimates of the aerodynamic properties in the event of large regions of separated flow. DES and LES, unlike Reynolds-Averaged Navier-Stokes (RANS) turbulence models, actually include estimates of the viscosity of the fluid rather than assuming that the fluid has zero viscosity. This provides a more realistic representation of the behaviour of the fluid away from solid walls. Consequently, the number of equations to be solved increases and hence also the computational cost compared to RANS methods. Furthermore, since a CFD solver with DES or LES models becomes unstable if the computational cell sizes are too large, very fine grid resolution is required in the area where the off-body flow is to be modeled – increasing computational cost even further.

For simple bluff bodies with smoothly-varying geometric features and no sharp corners (like spheres and spheroids), flow at the stagnation point is characterized by a laminar boundary layer; as one moves downstream along the curve of the body, this laminar layer gradually

transitions to a more stable turbulent boundary layer and eventually the flow may separate from the solid surface. Surface roughness can dramatically reduce the drag by forcing an earlier transition to the turbulent boundary layer and hence moving the separation point further downstream along the curve of the body. This delay of separation causes lower pressure drag and lower overall drag. Nonetheless, the drag on this class of bluff bodies is composed of a significant amount of viscous drag as well as pressure drag.

Bluff bodies with sharp edges, such as cargo containers on the other hand, have predetermined separation points (the sharp edges) and hence, depending on the orientation of the body, the drag on such bodies is mostly pressure drag. This is especially true if the body has no surfaces at an oblique angle relative to the freestream such as a box with a flat end directly into the wind or a flat plate broadside to the oncoming air. This case poses a great challenge to most state-of-the-art CFD solvers which have been optimized to resolve flow features within the boundary layer and neglect most features away from the body such as shed vortical structures that migrate downstream and could potentially affect pressure distribution over downstream parts of the body and hence the forces and moments acting on it.

One aspect of massively-separated flow which is in favor of the potential use of existing CFD solvers for predicting bluff-body aerodynamics is the fact that aerodynamic coefficients on bluff bodies are very weak functions of both Reynolds (Re) and Mach (M) numbers [Ref. 7]. Hence, one can use flow solvers written with numerical methods that are more suited to compressible flows (M > 0.2), to solve bluff-body flows in the incompressible region. Furthermore, the fairly recent development of DES methods that have in a short period come into widespread use in the CFD community, has opened the door to a solution of this difficult problem without incurring a large computational cost or a manpower investment in new CFD solvers. The reason for this is that the implementation of DES into existing flow solvers is very simple compared to that of LES. DES uses already-existing subroutines for calculating fluid viscosity and applies a simple grid-based filter – if a cell size is smaller than a pre-determined size, the viscosity is modeled and if it is larger than that threshold, viscosity is set to zero (the solver resorts to calculating only the Euler equations (a simplified version of the Navier-Stokes equations that neglect viscosity). LES, on the other hand uses complex spatial filtering techniques and more-complex turbulence model equations that are less trivial to program and add to existing CFD solvers. At Northern Arizona University a version of DES-SA has been implemented into the OVERFLOW flow solver. Even though OVERFLOW is a compressible code and more widely used for high-speed flows (the minimum speed for accurate computations using the compressible solver OVERFLOW is considered to be M = 0.2), the above comments regarding the insensitivity of bluff-body aerodynamics provide some preliminary confidence that OVERFLOW may well be able to predict the aerodynamics of the CONEX at speeds as low as M = 0.1 (60 knots at sea level).

## 1.2 Physical Details of the CONEX

The CONEX is a steel box equipped with skids for forklift manipulation. It has full doors at one end, corrugated sides, indented top edges and lift point lugs at the top corners. The flight test unit is shown in Fig. 2. The box dimensions of the test unit are 8.48 ft long by 6.11 ft wide by 6.41 ft high. The skids are 6 in high by 3 in wide with fork lift holes. Corrugations are 2 in wide by 1.5 in deep with 2 in separations. The weight, cg inertia and cg locations of two test configurations (empty and ballasted) are listed in Table 1. Body axes for these data are a right-

handed system with z positive down and x perpendicular to a long side. The cg location is given relative to the geometric center of the box.

**Table 1: Weight-Inertia Properties of the CONEX**

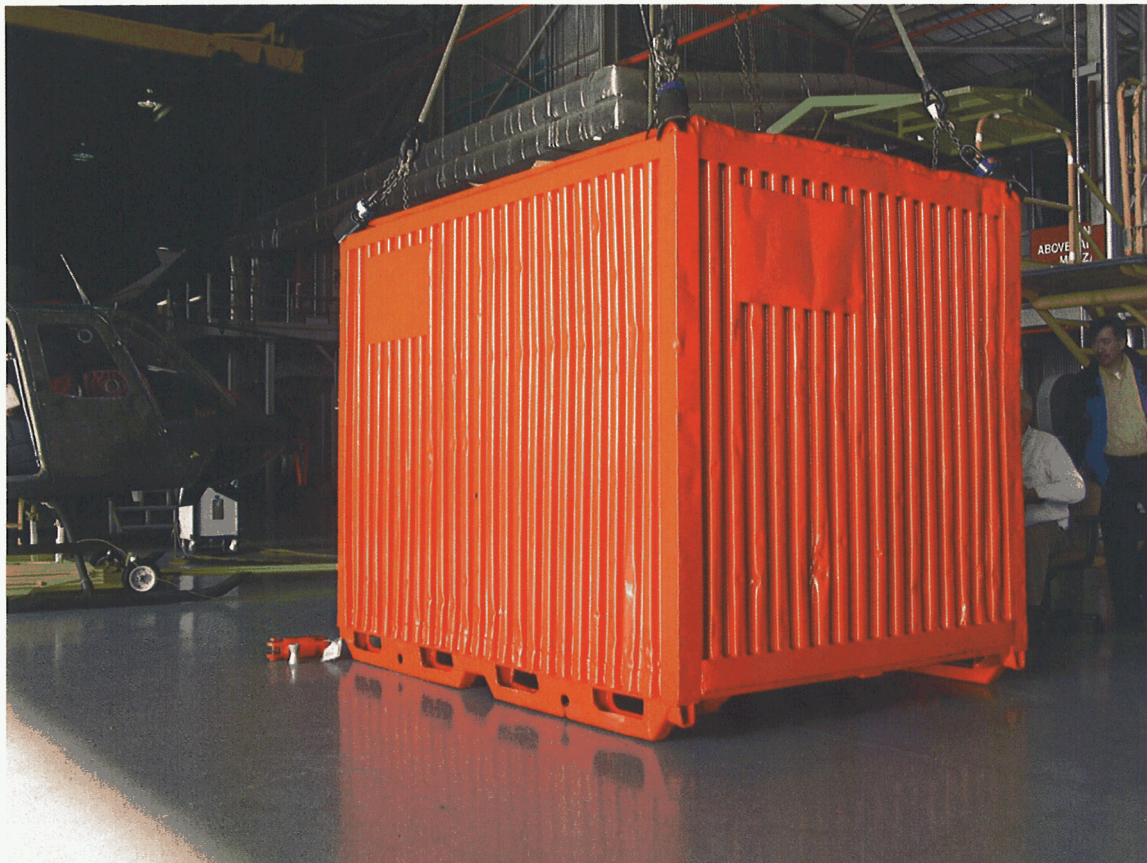|  | Units | Empty CONEX | Ballasted CONEX |
|---|---|---|---|
| Weight | lbs | 2156.9 | 4319.1 |
| Ixx | ft-lbs-sec$^2$ | 1001.5 | 1382.3 |
| Iyy | ft-lbs-sec$^2$ | 763.7 | 993.0 |
| Izz | ft-lbs-sec$^2$ | 933.3 | 1254.6 |
| x cg location | ft | 0.09 | 0.05 |
| y | ft | 0.15 | 0.08 |
| z | ft | 0.37 | 1.32 |



*Figure 2. Photograph of the CONtainer EXpress (Broad Side on the Left)*

## 2. COMPUTATIONAL SETUP

### 2.1 CFD Solver

OVERFLOW was the CFD code chosen for this study. This choice was based on the code's ability to perform arbitrary body motions that, although not employed in the work reported here, will be needed for the second phase of the CFD study that will focus on the moving CONEX. The major disadvantage of OVERFLOW for this study is the fact that it is a compressible code and hence may exhibit numerical instability at Mach numbers below 0.2 in the speed range of interest for slung loads. However, since this is a bluff-body problem and the force and moment coefficients for bluff bodies are insensitive to Mach number, we opted to use OVERFLOW and perform the simulations at M = 0.2. The assumption of Mach number invariance was checked with a series of simulations to be discussed here in section B. A prior study of the CONEX [Ref. 2] indeed showed that the 2D aerodynamics is invariant with Mach number.

### 2.1.1. OVERFLOW background and details

OVERFLOW was first developed with fixed wing applications in mind [Ref. 8, 9]. However, due to its ability to simulate arbitrary body motion, various versions of the code have been developed and applied to stores separation and rotorcraft [Refs. 10, 11].

OVERFLOW provides options for a number of aspects of the computational setup that can be selected and / or adjusted to suit the application. These include (1) turbulence model selection, (2) temporal discretization and time-stepping schemas (time integration), and (3) spatial discretization of the grids used to represent the physical model, as well as a variety of parameters such as: dissipation schemes and constants, matrix inversion schemes etc. The remainder of this section is devoted to outlining and justifying the OVERFLOW options chosen for this study.

For the present work, OVERFLOW version 2.0y was used. Like other versions of OVERFLOW, 2.0y solves the compressible form of the RANS equations using an implicit finite difference approach with structured overset grids. The code has various numerical techniques suitable for unsteady flows as detailed in [Ref. 12].

OVERFLOW makes use of distributed parallel computing techniques to enable the timely solution of large grids on high performance compute clusters. After the user selects the number of compute nodes that will be used for the computation, OVERFLOW automatically decomposes the system of overlapping grids into subgrids. The number of subgrids may be manually adjusted or the codeis allowed to determine the optimum number of subgrids. For an HPC system comprised of homogeneous nodes (the same number and type of CPUs, equivalent amount of RAM), the subgrids are sized in such a way that all nodes are assigned an equal number of gridpoints. If the number of subgrids is too large, the computational effort associated with inter-node communication (exchange of information between nodes that contain sections of a grid that was split during grid partitioning) may become a bottleneck during the simulation. This feature in OVERFLOW has been enhanced and the latest version typically calculates an optimal subgrid size. The subgrids are combined into a number of groups equal to the number of compute nodes. Each group is placed onto a separate processor and boundary information is

passed between the compute nodes at each time step/iteration. Both near- and off-body grids are partitioned in a similar fashion with the difference that the splitting of near-body grids is not allowed in the wall-normal direction. This feature is planned for future versions of the code. The result of the grid partitioning is that any given node can potentially contain subgrids of near-body grids as well as parts of off-body grids. The code is scalable, well load balanced and very efficient, resulting in a low turn around time for a given computation.

Although the grids used in this study are in dimensions of ft, internally OVERFLOW uses nondimensional numbers. The nondimensional calculations and input files used during this work are included in the appendices.

### 2.1.2. Brief summary of the Navier-Stokes equations

Although a detailed description and derivation of the Navier-Stokes is outside the scope of this report (for a complete treatment, refer to Ref. 13), it was felt that a brief description was needed to clarify certain terms used in the following sections. As applied to a time-marching CFD solution, the Navier-Stokes equations may be represented by the following equations:

$$\frac{\partial U}{\partial t} = J - \frac{\partial F}{\partial x} - \frac{\partial G}{\partial y} - \frac{\partial H}{\partial z} \qquad (1)$$

The term on the left contains the time derivatives and is often referred to as the left hand side (LHS) and those on the right hand side (RHS) contain the spatial derivatives. J is the source term (in this case it is zero since there are no body forces or volumetric heating) and U, J, F, G and H are defined as follows:

$$U = \left\{ \begin{array}{c} \rho \\ \rho u \\ \rho v \\ \rho w \\ \rho(e + \frac{V^2}{2}) \end{array} \right\} \qquad (2)$$

16

$$F = \left\{ \begin{array}{c} \rho u \\[2mm] \rho u^2 + p - \tau_{xx} \\[2mm] \rho v u - \tau_{xy} \\[2mm] \rho w u - \tau_{xz} \\[2mm] \rho(e + \dfrac{V^2}{2})u + pu - k\dfrac{\partial T}{\partial x} - u\tau_{xx} - v\tau_{xy} - w\tau_{xz} \end{array} \right\} \qquad (3)$$

$$G = \left\{ \begin{array}{c} \rho v \\[2mm] \rho u v - \tau_{yx} \\[2mm] \rho v^2 + p - \tau_{yy} \\[2mm] \rho w v - \tau_{yz} \\[2mm] \rho(e + \dfrac{V^2}{2})v + pv - k\dfrac{\partial T}{\partial y} - u\tau_{yx} - v\tau_{yy} - w\tau_{yz} \end{array} \right\} \qquad (4)$$

$$H = \left\{ \begin{array}{c} \rho w \\[2mm] \rho u w - \tau_{zx} \\[2mm] \rho w v - \tau_{zy} \\[2mm] \rho w^2 + p - \tau_{zz} \\[2mm] \rho(e + \dfrac{V^2}{2})w + pw - k\dfrac{\partial T}{\partial z} - u\tau_{zx} - v\tau_{zy} - w\tau_{zz} \end{array} \right\} \qquad (5)$$

$$J = \left\{ \begin{array}{c} 0 \\ \rho f_x \\ \rho f_y \\ \rho f_z \\ \rho(u f_x + v f_y + w f_z) + \rho \dot{q} \end{array} \right\} \qquad (6)$$

In the above equations, u, v and w are the three components of the velocity vector and $\tau$ is the shear stress which may be related to the fluid viscosity.

### 2.1.3. Turbulence model selection

OVERFLOW has several options for modeling boundary layer turbulence. For the studies in this project the Baldwin-Barth (BB) [Ref. 14], Spalart-Allmaras (SA) [Ref. 15], kw, kw-SST [Ref. 16] and the Detached Eddy Simulation (DES) method based upon the SA formulation first implemented by Strelets [Ref. 17] were used. The boundary layer was assumed to be fully turbulent and no trip lines were provided. Most problems in aerodynamics that involve external flow with little separation can be accurately modeled by making the assumption that the role of viscosity in velocity profiles is limited to the direction normal to the wall. This is true for most situations since the velocity profile is very steep in the wall-normal direction (across the boundary layer) and changes less abruptly as a function of distance in all other directions. However, when the flow is massively separated, the flow is more three-dimensional and the local velocity profile changes with similar orders of magnitude in all directions. This necessitates the use of viscous terms in all directions.

With the exception of the DES-SA implementation, the flow in the background grids was assumed inviscid and hence required no turbulence model. DES-SA simulations however, used all viscous terms (including cross terms) for off-body grids. The near-body grids were run in thin-layer RANS mode (only viscous terms normal to the wall were included) for all steady-state and unsteady calculations. This may be justified in light of the fact that the DES-SA model switches from solving the thin-layer RANS equations to solving the fully viscous off-body grids very close to the body. This is in line with Spalart's recommendation of using thin-layer RANS for the near-body grids and fully-viscous grids for the off-body [Ref. 18].

### 2.1.4. Temporal discretization and time-stepping schemas

Simple 1st order time-stepping was employed for most runs. In some cases up to five 2nd order Newton subiterations were performed but this showed negligible improvements in integrated forces and moments when compared to simple 1st order time-stepping (Euler integration with fixed derivative over the time step). A subiteration uses the result of the integration over a time step as input to re-evaluate the same time step a number of user-specified times before proceeding to the next time step. The subiterations can be first-order, or

alternatively use a second-order polynomial to represent the time from the start to the end of the time step.

Various attempts were made to use the unsteady low Mach number preconditioner built into OVERFLOW 2.0y for Mach number below 0.2. In order to ensure numerical stability and solution convergence (at least two orders of magnitude reduction in residual errors between time steps), a dual time step scheme was needed with multiple (more than three) Newton subiterations. In some cases up to 80 subiterations were required per time step. This is prohibitively expensive in terms of solution time and hence our attempts to include preconditioned solutions in this report were abandoned.

### 2.1.5. Spatial discretization of the grids, and other numerical settings

The right hand side (RHS) of the Navier-Stokes equation was solved with a 2nd or 4th order central difference scheme for the spatial discretization. Smoothing is required due to odd-even decoupling; 4th order smoothing away from shocks and 2nd order smoothing in the presence of shocks. Since there are no shocks present in the low Mach number flows studied here, the 2nd order smoothing was turned off (DIS2=0.0). It should be noted that the 4th order smoothing value (DIS4) has a strong effect on the skin friction and hence the drag force calculation. The OVERFLOW default value of DIS4=0.04 in general provides for a very stable solver, but may lead to erroneous drag values. Most of the studies reported on here used DIS4 values smaller than 0.04 – as low as 0.01.

For the left hand side (LHS) a scalar pentadiagonal scheme was used (see page 26 in Ref. 8). The pentadiagonal scheme has the advantage of being fast and requires very little memory. Its drawback however, is that it is the least stable of the numerical methods in OVERFLOW. This numerical instability may be kept in check by adding artificial dissipation; for this work, the TLNS3D scalar dissipation scheme was used.

### 2.2 Mach Number Invariance

The concerns previously expressed regarding the potential error introduced by performing the current simulations at low Mach numbers with a compressible solver, was checked by repeating the same simulation (BB turbulence model, side slip angle = 0 deg) at three Mach numbers. The results shown below indicate that Mach number has a small effect on the integrated drag force. This finding, coupled with the earlier 2D results in Ref. 2 give us confidence in the results provided by OVERFLOW at low Mach numbers.

**Table 2. Mach Number Study (Average over
30,000 Time Steps Using the
BB Turbulence Model with Side Slip Angle and
Pitch Angle at Zero Deg)**

| Mach number | Drag Force Coefficient $ft^2$ |
|---|---|
| 0.2 | 58.39 |
| 0.25 | 57.42 |
| 0.3 | 58.02 |

## 2.3 Benchmarks on Various Clusters Used

Calculations were performed on small clusters of dual-CPU nodes at NAU and the Columbia high-performance computer located at NASA Ames. Unsteady calculations are very compute-intensive and the performance statistics of these clusters using OVERFLOW are shown in Table 3. The benchmark study used a CONEX grid consisting of six million grid points.

**Table 3: Benchmarks for High Performance Computers (HPC) Used in this Study**

|  | Columbia[1] | Columbia[2] | NAU xbot | NAU phoebe |
|---|---|---|---|---|
| CPU | Itanium2 | Itanium2 | Apple PPC 970 | AMD Opteron |
| Clock speed (GHz) | 1.6 | 1.6 | 2.5 |  |
| RAM per CPU (GB) | 2.0 | 2.0 | 1.25 | 2.0 |
| Compiler | Intel | Intel | XLF / gcc | PGI |
| Interconnect | NUMA[3] | NUMA | GigE | GigE |
| CPUs used | 36 | 36 | 4 | 16 |
| Performance[4] | 0.15 | 0.12 | 2.81 | 0.53 |
| Time per unsteady solution[5] | 7.5 | 6.0 | 140 | 26.5 |

[1]Save every 100 steps
[2]Save every 500 steps
[3]Non-Uniform Shared Memory – each 512 CPUs share 1 TB of RAM
[4]Units of measure: $\mu s.step^{-1}.gridpoint^{-1}$
[5]Wall hours for 30,000 time steps using a grid with 6E6 points

The grid used in this benchmark sufficed to represent the CONEX with skids and top edge indentations. To include the corrugations, grid size would increase to an estimated 20 million points and time requirements would increase correspondingly. The number of 30,000 time steps was chosen so that averages taken over the last 20,000 time steps did not change when the iteration count was increased.

A complete table of the static aerodynamics of the CONEX every 5 deg in angle of attack over the interval [-90°, 90°] and in sideslip angle over [0,180°] (taking advantage of symmetry rules around beta = 0 for the CONEX) would require 1369 cases. On Columbia, where the computations were distributed among 36 CPU's, this would require some 36*6*1369 = 296000 CPU hours. However, for the static aerodynamics it is reasonable to use the steady flow Navier-Stokes equations that would run 6 times faster (only 5000 time steps are needed for convergence) and use 49000 CPU hrs. In terms of wall clock time-to-job-completion, 343 days are required on Columbia, which can be reduced to 57 days by using the steady flow equations, and further reduced to 5.7 days by running 10 cases simultaneously (Columbia has 10480 nodes). The university cluster, Phoebe, would require 4.4 times as much wall clock time as Columbia. A complete table using steady flow would require 252 days.

In the moving CONEX CFD tasks, some interval of real time would be simulated. An approximate rule is that the real time step should be equivalent to 0.1 deg of rotation or less for stability. Assuming rotation rates up to 2 Hz are to be simulated, then, the required real time step is 0.000139 sec and 30000 dimensionless time steps would correspond to 4.2 secs of real time. Using the numbers in Table 3, then the 3D unsteady flow calculation would require 1.4 hrs per sec of real time on Columbia and 6.3 hrs on Phoebe.

These estimates for CPU resource requirements to study the steady and unsteady flow around the CONEX and document static or spinning or forced oscillation aerodynamics of the CONEX using 6 million grid points and the OVERFLOW code are considered ordinary for the typical task on Columbia. While some production tasks would not be feasible on a small university cluster, such clusters are valuable in development of the computational setup and for limited amounts of data.

## 2.4 Grids

The CONEX is a simple 3D box with skids, top edge indentations and sidewall corrugations. The grids used in the present study represent the box alone or the box with skids and top edge indentations. Surface corrugations were not included since it was expected that corrugations would have a smaller effect on forces and moments than details at the extremities, and because the CONEX has predominantly separated flow around it, and because it might have required a much larger grid, of order 20 million points. These grids consist of one or more near-body grids (depending on the complexity of the body) embedded in a number of Cartesian off-body grids. The latter are automatically generated by OVERFLOW at runtime.

The near body grids were generated using Chan's hyperbolic grid generation technique known as HYPGEN along with the graphical front-end software OVERGRID [Ref. 19]. Forces and moments were calculated during the simulation with OVERFLOW's built-in FOMOCO utilities [Ref. 20] that integrates the surface pressures and skin friction.

The simplest of the grids (Original) was a rectangular box with sharp edges consisting of 115,920 near-body grid points and about 1E+6 total grid points including far-field cartesian grids (depicted in Fig. 3). The next grid (Refined) was a refined version of the first grid with the two

singularities cut out and replaced with two rectangular patches (see Figs. 4 to 6). The Refined grid featured enhanced grid clustering around the edges and slightly rounded corners and it consisted of three near-body grids; the main, refined grid with holes at the poles and two flat patches that covered the holes. The last grid (shown in Fig. 3) consists of twelve sub-grids that define the entire geometry of the main vessel as well as the skids and the top indentations (Skids).

**Table 4: Summary of Computational Grids Used in OVERFLOW**

| Grid | NB grids | NB points | Viscous layers | Name | Main features |
|------|----------|-----------|----------------|------|---------------|
| 1 | 1 | 1.16E+5 | 21 | **Original** | Simple box, sharp corners, axis point (singularity) |
| 2 | 3 | 1.24E+6 | 31 | **Refined** | Refined version of **Original**; same basic shape. Singularity removed and covered with rectangular patches, smoothed and rounded corners |
| 4 | 12 | 2.13E+6 | 55 | **Skids** | Sharp corners but includes skids and indentation around the top of the CONEX |

Further differences in the three grids are also evident from Table 4. The number of near-body grid points varied between 1.16E+5 to 2.13E+6 from the Original to the grid with skids. In addition to the refinement of the surface grid, the volume grid was also refined more extensively, with 21 layers used in the Original grid, 31 for the Refined grid and 55 layers for the grid with skids. In all cases, however, the first three viscous layers on the body were equidistant from each other to ensure accuracy in shear-stress and hence drag calculations and all the grids were generated to ensure a y+ value smaller than 1.0. The near-body grids extended 1ft into the computational domain, or 1/6 of the shortest (characteristic) body length of 6.11ft.
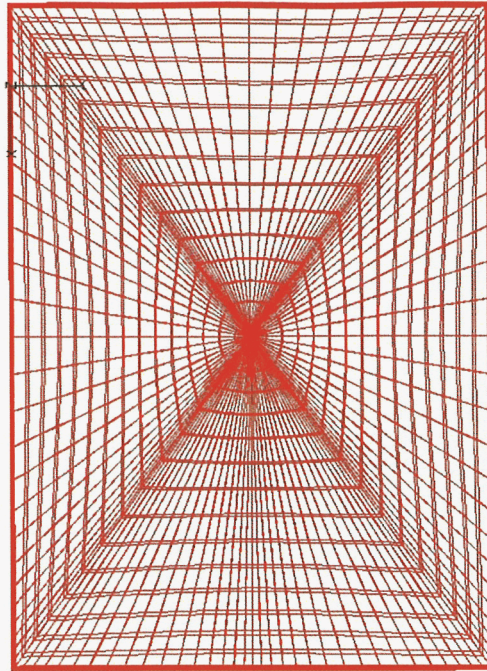
*Figure 3. Unmodified Surface Grid with Polar Boundary Condition at the Axis Of Rotation*
*– **Original** Grid*
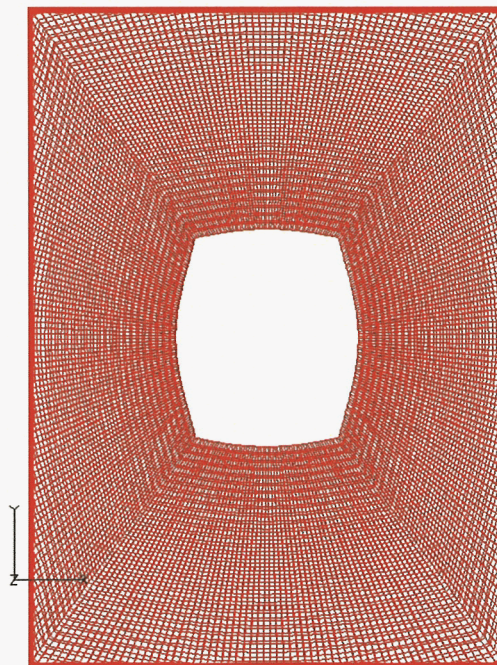


*Figure 4. Hole Cut Removed the Pole (Axis Boundary Condition);*
*Surface Refined in two Directions - Refined Grid*
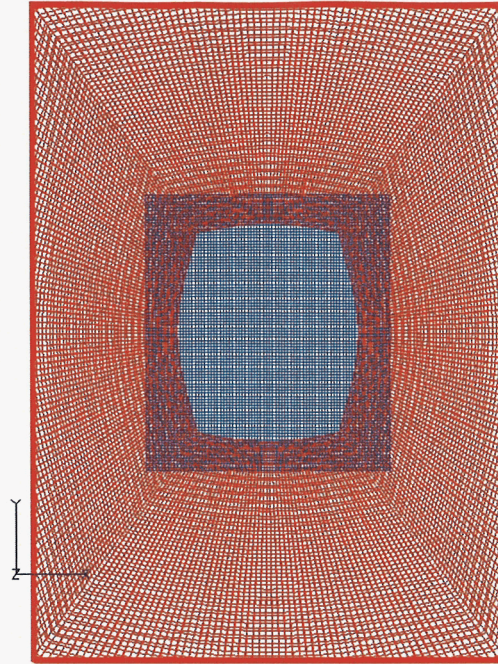
*Figure 5. Patch to Cover Hole over Former Axis Point – **Refined** Grid*
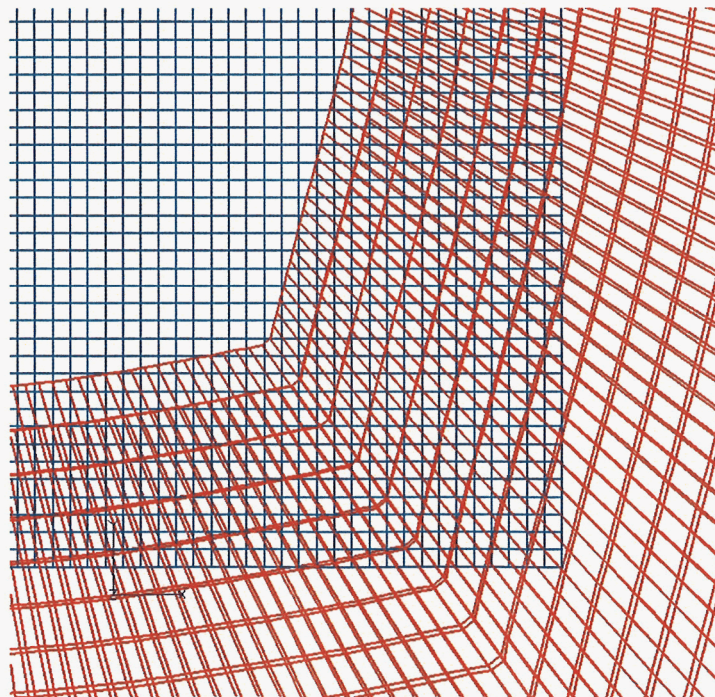


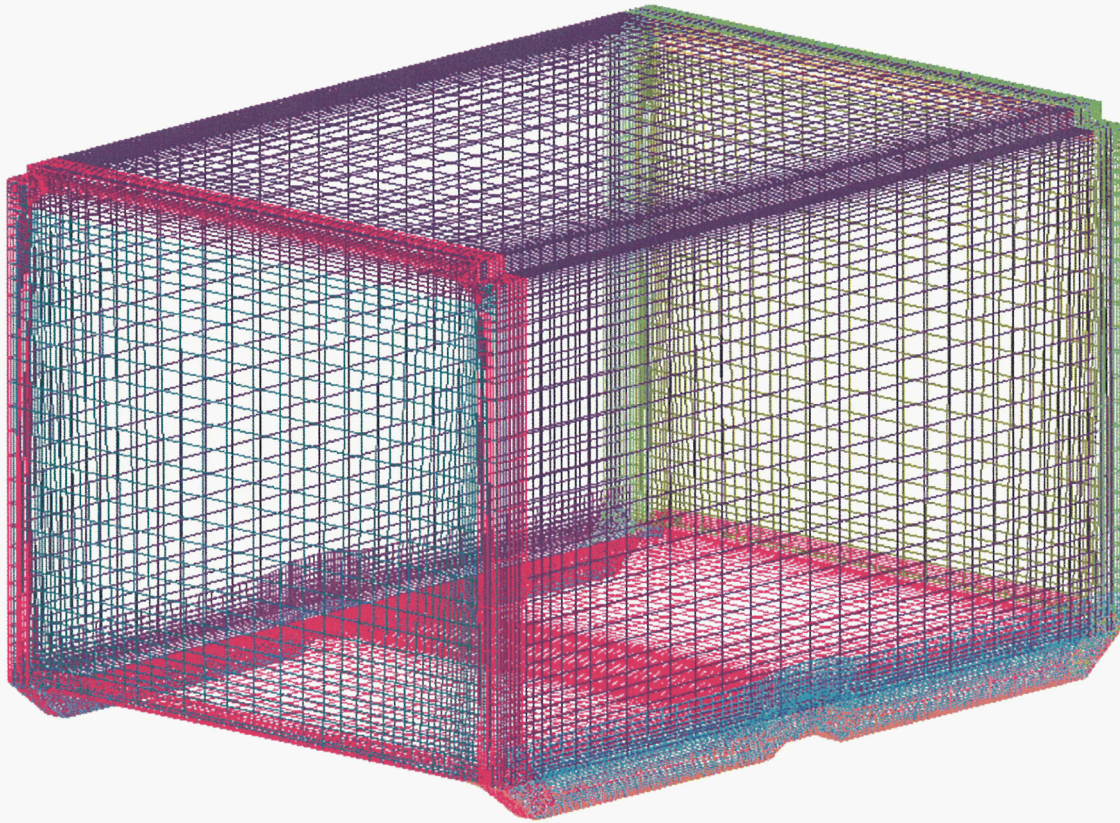*Figure 6. Close-Up of Patched Hole – **Refined** Grid*

*Figure 7. Complex Grid Depicting Skids as well as Top Indentations*

## 3. RESULTS–VALIDATION OF CFD AGAINST WIND TUNNEL DATA

A summary of the data presented in this section is shown in Fig.8. Steady-state simulations were only performed on the Original grid and with varying side slip angle and fixed angle of attack (0 deg).
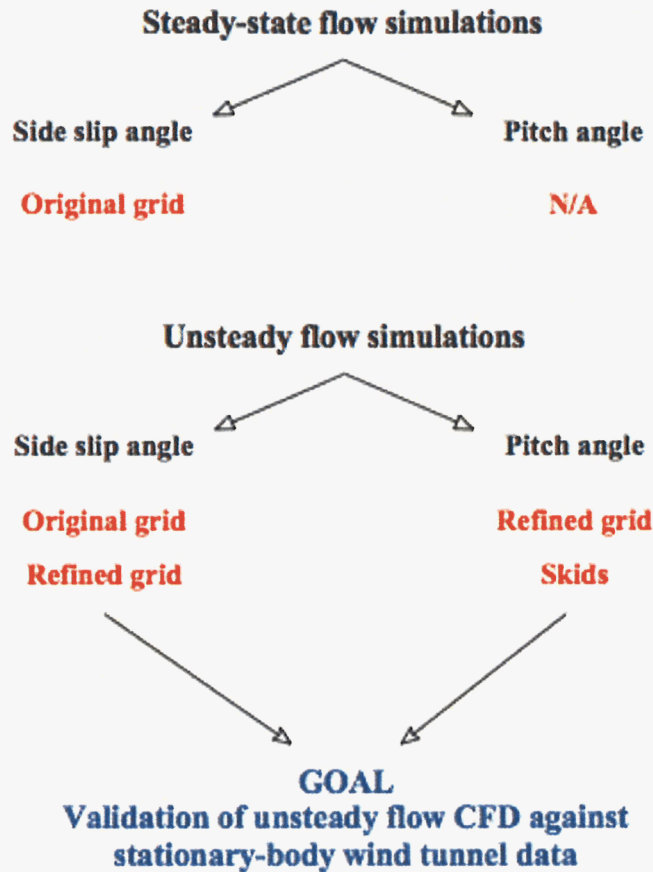
**Steady-state flow simulations**

Side slip angle                              Pitch angle

Original grid                               N/A

**Unsteady flow simulations**

Side slip angle                              Pitch angle

Original grid                            Refined grid

Refined grid                               Skids

**GOAL**
**Validation of unsteady flow CFD against**
**stationary-body wind tunnel data**

*Figure 8. Summary of the Simulations Performed and Grids Utilized*

Unsteady flow simulations repeated the study of variable side slip angle at constant angle of attack using the Original grid but also studied the effect of grid refining. The effect of varying angle of attack at constant (0 deg) side slip angle was studied with both the Refined grid and the grid containing skids. A grid with skids was utilized since the skids introduce a significant asymmetry about aoa = 0 deg in the variation of the aerodynamics with aoa which could not be captured by a grid representing only the box.

In the following it is convenient to give the aerodynamics as force and moment divided by dynamic pressure (units are $ft^2$ and $ft^3$), or equivalently, as coefficients times area (A) and volume (AL), respectively, e.g., $C_DA$, $C_nAL$, etc.. In this form, the aerodynamic data apply to all airspeeds.

Numerical values for the data of this section are given in Tables 6 to 14 in Appendices C through G.

**3.1 Steady-State CFD Results (Original Grid)**

**3.1.1. Drag, side force, yaw moment vs. side slip angle**

Steady-state calculations differ from unsteady flow calculations in that the solutions do not represent time-accurate flow fields. The grids are allowed to converge to a steady solution

by using local time-stepping, which implies that various sections of the flow field in the final converged solution represent different instances in time. The value of steady-state simulations for massively-separated flow is somewhat dubious because of the large differences in variables such as the velocity components at a given point in space as a function of time. The omission of details such as skids and corrugations in the grids adds to the shortcomings of the steady-state simulations presented in this section. Nevertheless, computational time requirements were relatively low and the results were expected to provide a first approximation to the wind tunnel which could be used, for example, to investigate the choice of turbulence model.

The first step in our validation was against wind tunnel (WT) data previously collected at the Technion-Israel Institute of Technology for the stationary CONEX [Ref. 3]. The WT data was collected using a detailed CONEX model with skids and corner indentations as well as side-panel corrugations (see Fig. 2), while the CFD data was computed for a box without details. Four turbulence models were evaluated, namely Baldwin-Barth, Spalart-Allmaras, kw and kw-SST (see Appendix C for a complete listing of CFD results). The latter two models are two-equation models that were developed to better resolve shear layers and regions of massively-separated flow. All steady-state CFD results presented in this section are at 0° angle of attack and used the Original grid. The other grids were used only for unsteady flow simulations. The wind-tunnel (WT) force and moment components were found to be periodic every 180° in sideslip angle and related every quadrant by symmetry rules. Hence, the CFD analysis was set up to calculate forces and moments in the first quadrant every 5° in sideslip angle from 0° to 90° with aoa set to zero. The CONEX was maintained at a constant sideslip angle (b) and with the solver set to steady-state mode, 4,000 time steps were calculated and the average taken. Strictly speaking, one expects the flow variables of a steady-state solution to converge to a single value; however in this case due to the nature of the flow there were still large changes in primitive variables (velocity components, density) around a mean value as a function of the time step. Time step in this instance (steady-state flow simulation) therefore does not refer to a physical instance in time, but a computationally-expedient choice of time step that results in a converged solution.

*Steady-state drag vs. side slip angle*

Fig 9 compares the steady-state drag for the different turbulence models. All four turbulence models predict similar CDA at sideslip angles between 30° and 75°, but some differences arise at low and high sideslip angles (broad side and narrow side to the wind respectively). BB appears to be the only model that replicates all the general features of the wind-tunnel data, albeit somewhat offset from the measured data (two minima; one between 5° and 15° and the second between 75° and 90° and one maximum value between 35° and 45°). The two-equation models fare the worst with kw exhibiting the highest discrepancy with WT data at most sideslip angles studied. It does appear that kw-SST improves on the performance of kw. Performance of the four turbulence models is very similar in the intermediate range of sideslip angles (between 30° and 75°). However, BB provides the best fit to the drag data based on the average % deviation from wind tunnel data (Table 5). In this range of sideslip angles, viscous drag due to skin friction plays a more significant role in the overall drag value because a significant surface area of the CONEX is at an oblique angle to the wind. Closer to 0° and 90° sideslip angle, pressure drag dominates.

27
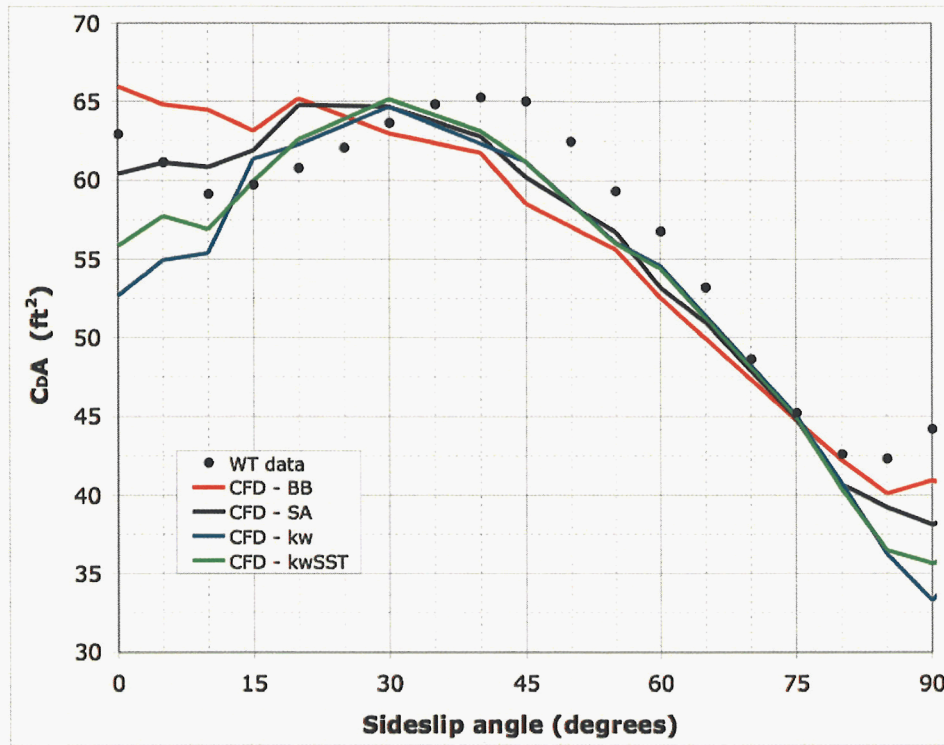
*Figure 9. Steady-State Drag as a Function of Side Slip Angle - Compared to Wind Tunnel Data*

*Steady-state side force vs. side slip angle*

For the prediction of side force (Fig. 10 the worst predictor is the kw model that deviates from wind tunnel data both at low and high sideslip angles. The kw-SST model does improve on this performance, but results are as good as and no better than that predicted by the one-equation models (BB and SA). Between 60° and 90°, all models fail to accurately follow the sharp decline in side force as a function of increasing side slip angle measured in the wind tunnel.
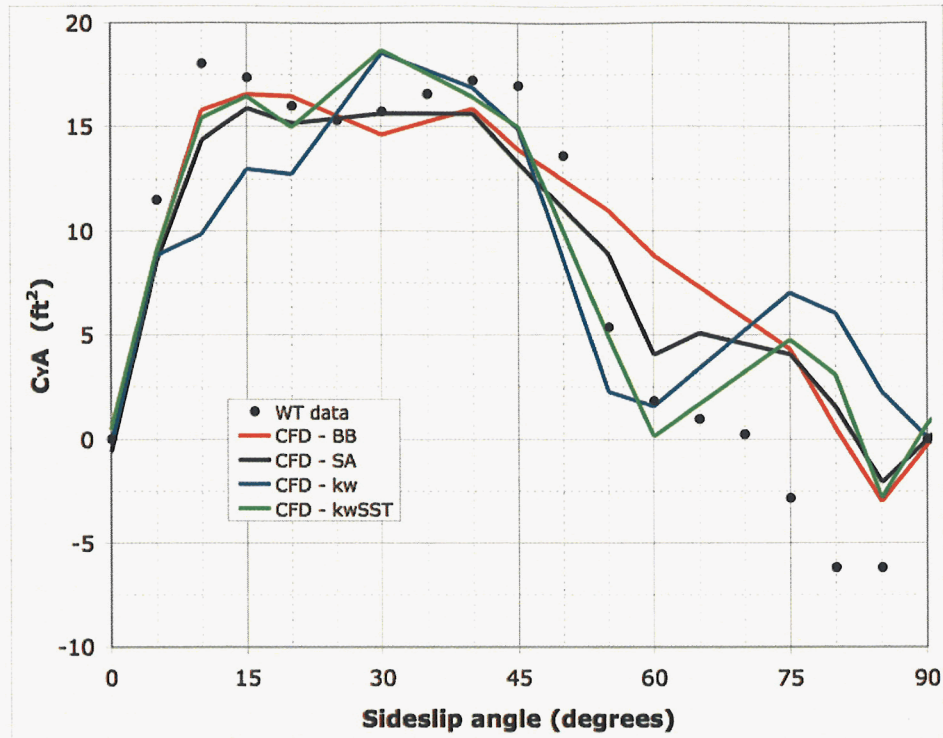
*Figure 10. Side Force as a Function of Side Slip Angle – Compared to Wind Tunnel Data*

The two-equation models follow the wind tunnel data fairly accurately up to 60° but then start to deviate significantly at higher side slip angles.

The force magnitude in the Y direction (side force) is about a third as large as the drag force (Fig. 9); hence any inherent inability of a turbulence model to predict forces on bluff bodies will be more pronounced in the side force. Even though it exhibits large deviations from wind tunnel data at high and low side slip angles, the kw turbulence model has proven to be the best predictor of CYA according to the error analysis presented in Table 5.

*Steady-state yaw moment vs. side slip angle*

In the prediction of the yaw moment (Fig. 11), the one-equation models once again provide a better estimate of wind tunnel data. CFD predictions are accurate up to side slip angle = 45° but at higher side slip angles all the turbulence models under-predict the yaw moment. The trends and location of the peaks in CNAL, however, are all predicted. The kw-SST turbulence model again proves a better overall predictor of yaw moment than the kw model.

These results are encouraging since the yaw moment has a strong influence on the onset of spinning instability of the CONEX in flight. Future work will focus on the unsteady aerodynamics of the moving CONEX and the eventual prediction of the onset of instability; hence the accurate yaw moment predictions in this work are of paramount importance.
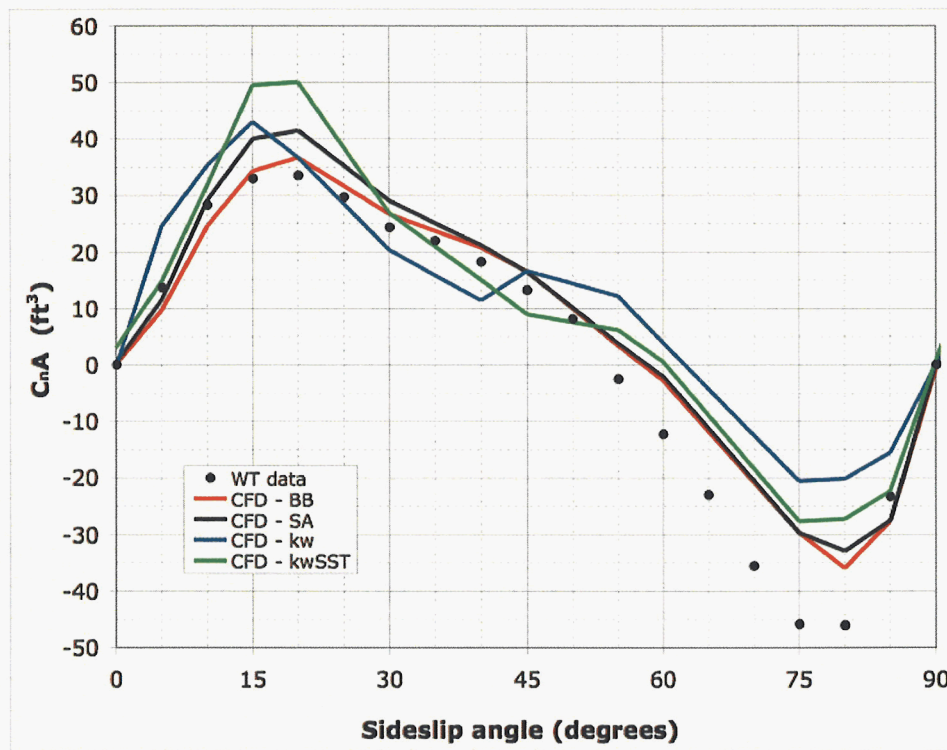


*Figure 11. Steady-State Yaw Moment vs. Side Slip Angle - Compared to Wind Tunnel Data*

The numbers bear out the main conclusion made earlier in the discussion; i.e. the one-equation turbulence models provide a better prediction of wind tunnel data and kw-SST provides a better fit than kw. The Baldwin-Barth turbulence model gave the best overall results (see Table 5 below).

### 3.1.2. Summary of steady-state CFD validation

In summary, the root mean square (RMS) error of the four turbulence models is presented in Table 5. There is no single turbulence model that stands out as the best performer of all the measured forces and moments, but on average the Baldwin-Barth model gives the closest agreement between CFD and wind tunnel results.

**Table 5: RMS Error between Steady-state CFD Predictions and Wind Tunnel Data**

| Turbulence model | $C_DA^a$ | $C_YA^b$ | $C_nAL^c$ | Average[d] |
|---|---|---|---|---|
| | % error | | | |
| BB | 0.55 | -7.58 | -8.92 | 5.68 |
| SA | 0.63 | -5.73 | -11.75 | 6.04 |
| kw | 5.16 | -3.51 | -24.18 | 10.95 |
| kw-SST | 4.12 | -4.92 | -20.53 | 9.86 |

[a]Expressed as a percentage of the average wind tunnel $C_DA$
[b]Expressed as a percentage of the maximum wind tunnel $C_YA$
[c]Expressed as a percentage of the maximum wind tunnel $C_nAL$
[d]Average of the absolute value of % error for $C_DA$, $C_YA$ and $C_nAL$

### 3.2 Unsteady Flow CFD Results

Given the encouraging results of the steady-state simulations, the next step was to perform unsteady flow simulations since the end goal of this report is the validation of the unsteady flow code against stationary-body wind tunnel data. The results of these unsteady flow simulations are presented in this section. Each data point is the average of the last 20,000 time steps of a total of 30,000 time steps.

Sample time histories of the aerodynamic components are shown in Fig. 12. All components vary continually over ranges which are ±6% (drag) to ±45% (lift) of the maximum value of the component in the wind tunnel data. Autocorrelations are shown in Fig. 13 vs. reduced frequency and exhibit common maxima at two frequencies. The first common peak occurs in the range of 0.16 to 0.19 and the second common peak occurs in the range of 0.32 to 0.38. These are presumably principal frequencies associated with periodic flow phenomena. The 2D aerodynamics investigated in [2] showed much simpler time-history characteristics with a single very strong autocorrelation peak at 0.70 associated with periodic vortex shedding and corresponding large amplitude sinusoidal oscillations of the forces and moments.
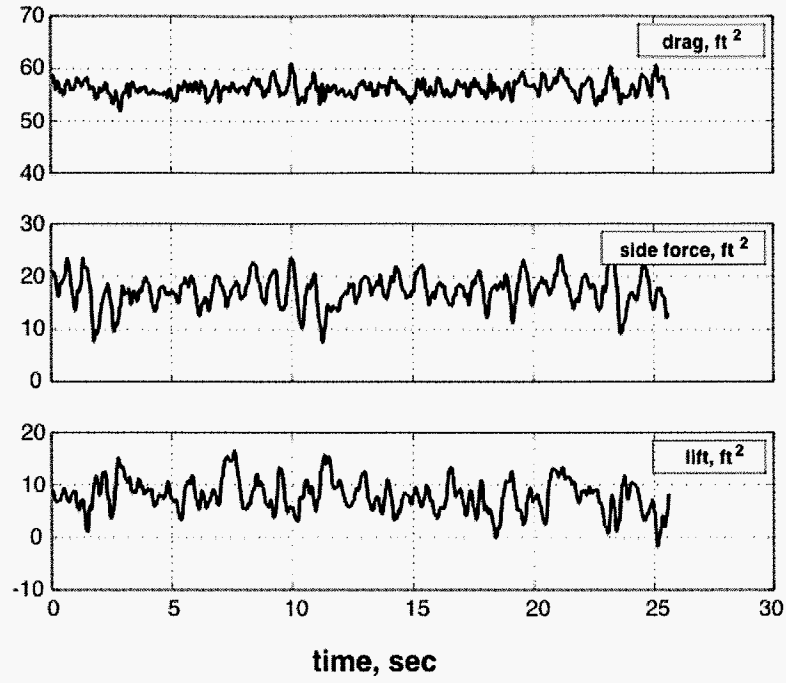
(a) forces

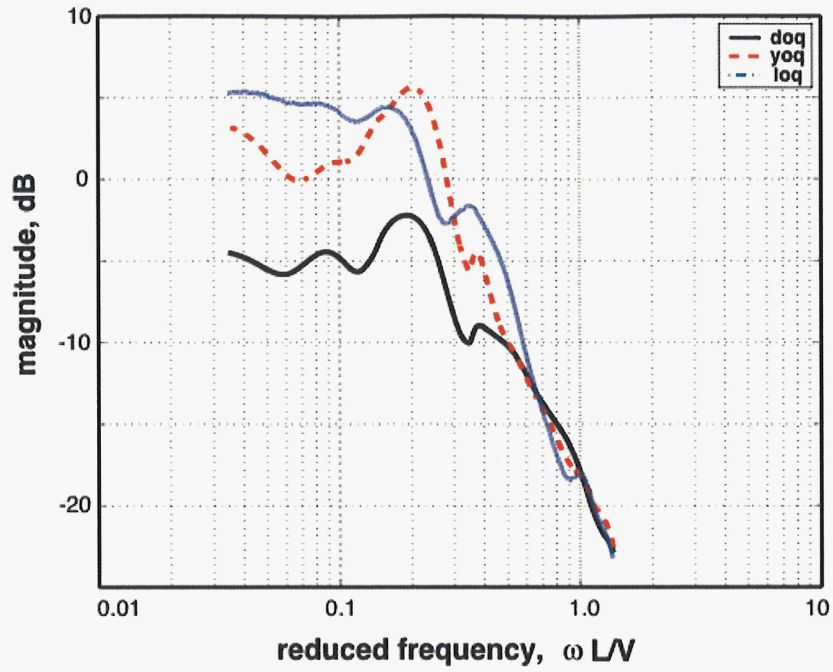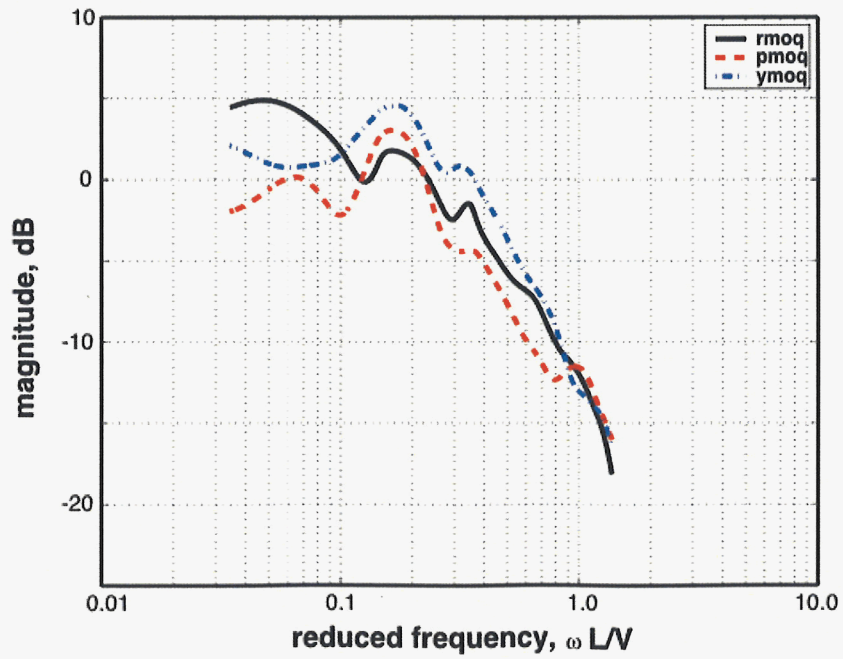*Figure 12. Unsteady flow time histories,* $\alpha = 0$, $\beta = 30$, $M = .2$, *original grid*
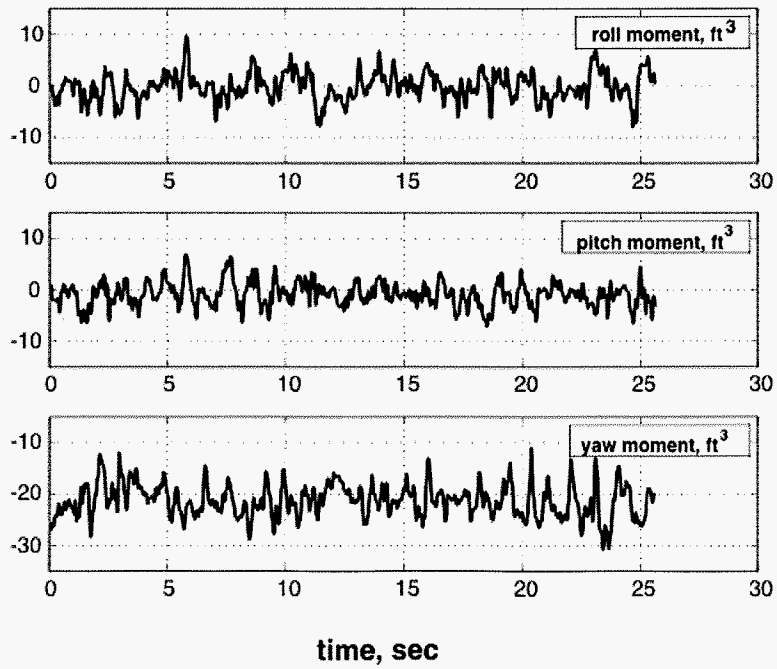


(b) moments

*Figure 12, cont.*



**(a) forces**

*Figure 13. Unsteady flow autocorrelations, $\alpha = 0$, $\beta = 30$, original grid*



**(b) moments**

### 3.2.1 Drag, side force, yaw moment vs. side slip angle (original and refined grids)

In this study, the CONEX was rotated around the Z axis (beta sweep) or the Y axis (alpha sweep) and maintained in successive fixed positions while OVERFLOW was run in time-accurate mode. This produced a time-varying flow field that allows one to gain insight into the major flow phenomena such as the size and frequency of vortex shedding, as well as the feedback effect of the vortex shedding on surface pressures. A typical run was performed for about 30,000 time steps with a dimensionless times step of 0.01 (equivalent to approximately 55 ms per time step – see Appendix A). In order to resolve fine-grained turbulence, Large-Eddy Simulation practitioners (LES) cite a time step of 1 ms (at 60kts) being necessary to resolve most of the important turbulent events [Ref. 21]. In this study a thin-layer RANS method based on the Spalart-Allmaras turbulence model was used. As mentioned before, simulationswere also done using the Spalart-Allmaras turbulence model re-coded into DES mode (DES-SA). This has a much smaller computational time requirement than LES methods and provides results with comparable accuracy. The drawback is that, due to the large time step used, we may not have resolved all of the important turbulent phenomena in the process.

The unsteady flow data for this section are listed in Table 10, Appendix D.The corresponding wind tunnel data are listed in Table 13, Appendix G. Data for the secondary components (pitching moment, roll moment, and lift) are included in Table 10 but are not discussed below. For a simple box these components are necessarily zero for all points with zero angle of attack and their departures from zero in the CFD results reflect the errors in the method. The results show small random errors with near-zero means and extremes that are at most 5% of the maximum magnitude of the component.

*Unsteady flow drag vs. side slip angle*

Figure 14 shows the drag force from unsteady CFD predictions as a function of side slip angle at aoa = 0°. The general trend of the wind tunnel data is well represented with a few notable exceptions; the peak in drag force observed in the wind tunnel at 40° is under-predicted and the minimum value at 85° is not captured at all. Large error bars [Ref. 6] in the wind tunnel data in the latter region is a possible mitigating factor in this mismatch of the CFD method.

The unsteadyflow CFD data represents the measured wind tunnel data more accurately than the steady-state CFD data. This is true especially at low side slip angles. However, unsteadyflow CFD also appears unable to accurately model the peak in drag force at 40° and while steady-state CFD was able to capture the minimum at 85°, unsteady CFD failed to do so.
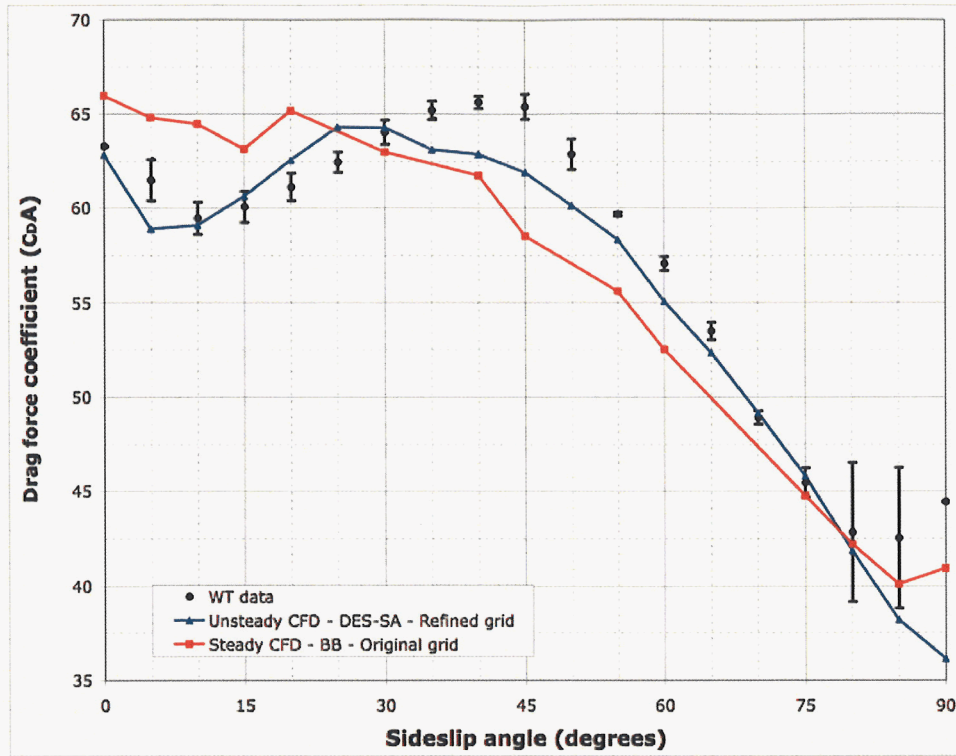
*Figure 14. Unsteady Flow Drag vs. Side Slip Angle - Compared to Wind Tunnel Data*

*Unsteady flow side force vs. side slip angle*

Side force predictions are shown in Fig. 15. Here the CFD method did not produce satisfactory results; CFD matches the wind tunnel data only at three points, $\beta = 0°$, $50°$ and $90°$. A possible explanation for this may be the fact that the side force magnitudes are much smaller than drag force for this and other bluff bodies, and hence the sensitivity for this measurement is smaller. Conversely, one would expect the wind tunnel side force data to also be more prone to error – based on the wind tunnel error bars however, it does not appear to be the case in this dataset.
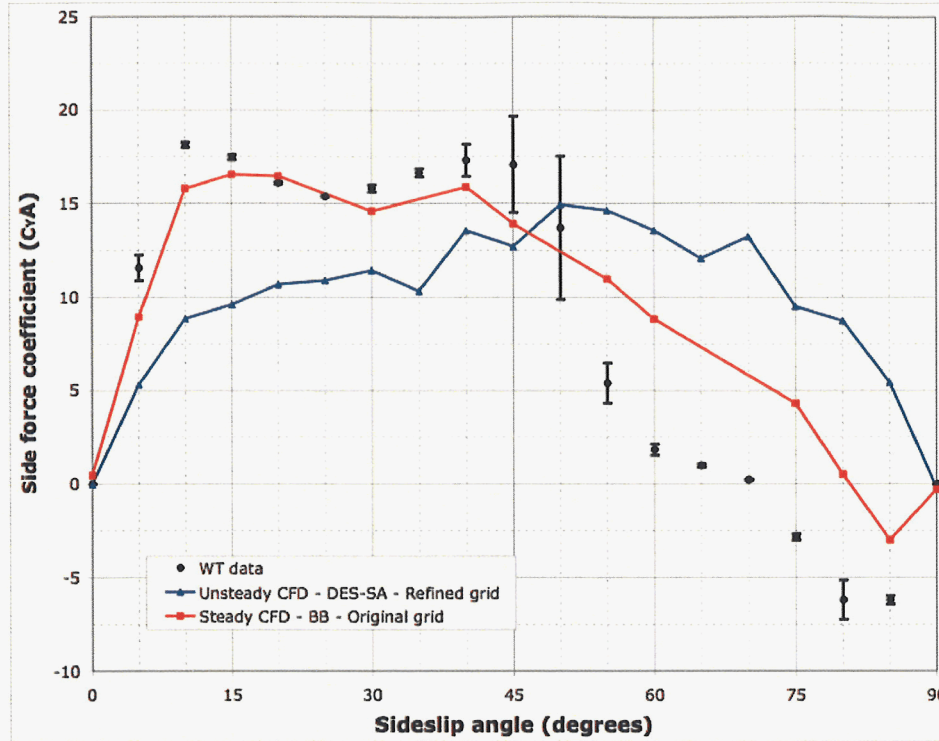
*Figure15. Unsteady Flow Side Force vs. Side Slip Angle - Compared to Wind Tunnel Data*

In the case of side force, the unsteady flow CFD method appears to provide a less satisfactory representation of wind tunnel data than the steady-state CFD method, in spite of the fact that a more refined near-body grid was used. Although results are not yet available for the CONEX with skids as a function of side slip angle, the possibility that the absence of skids in the CFD grids could account for this discrepancy has to be ruled a strong possibility. Unfortunately the effect on the side force of the grid with skids was not studied and this question remains unanswered at present. This points most likely to a deficiency in one of the original assumptions of this study, namely that the skids only have an effect on the forces and moments as a function of pitch angle and not as a function of side force.

*Unsteady flow yaw moment vs. side slip angle*

Figure 16 depicts the unsteady, time-averaged yaw moment predicted by DES-SA as a function of side slip angle. There is very good agreement with wind tunnel data between 0° and 50° and at 85° and 90°, but between 50° and 85° there is a noticeable discrepancy. The agreement of unsteady CFD results with wind tunnel data is improved over the entire range of sideslip angles when compared to steady-state CFD results.
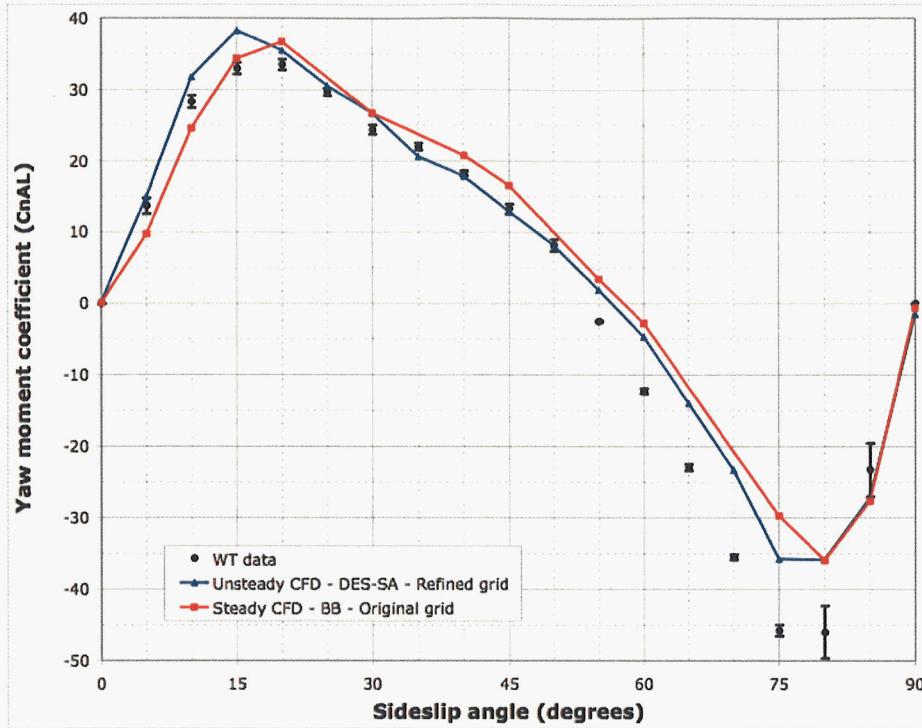
*Figure 16. Unsteady Flow Yaw Moment vs. Side Slip Angle - Compared to Wind Tunnel Data*

### 3.2.2 Drag, side force, yaw moment vs.angle of attack (refined grid and grid with skids)

The unsteady flow data for this section is listed in Appendix E. The corresponding wind tunnel data are in Table 14, Appendix G. The case that $\alpha = \beta = 0$ was repeated 8 times in order to examine solution scatter and provide the error bars (one standard deviation) in Figs. 17 to 19 for this case. Numerical results are given in Table 12, Appendix F. Standard deviations are just under 2 ft$^2$ for drag and lift and 3 ft$^3$ for pitching moment.

Drag, lift, and pitching moment data are presented in this section while the data for side force, roll- and yaw moments are omitted.

*Unsteady flow drag vs. angle of attack*

The drag force is plotted as a function of angle of attack in Fig 17. The wind tunnel data shows an asymmetry in drag force to the left and right of zero angle of attack. This is most likely the result of the presence of skids, rather than skin corrugations since the latter are symmetric with respect to the angle of attack. It should therefore be expected that the grid with skids would provide a better estimate of the drag as a function of angle of attack.

The grid with **skids** approximates the drag force accurately across the entire range of angle of attack studied. There is a slight negative offset compared to wind tunnel data, especially at negative angles of attack and at positive angles of attack exceeding about 45°. The peak at 45° is well captured by CFD simulation. The error bars on the CFD data indicate that it accurately represents the wind tunnel data at $\alpha = 0°$ within measurement error. In the absence of skids, drag

37

would be symmetric about aoa = 0°. The effects of the skids are seen as differences between drag at $+\alpha$ and $-\alpha\underline{=\alpha}$ in the wind tunnel data, with the largest such difference at +90°, and the CFD results capture this departure from symmetry. The **Refined** grid (no skids) resulted in a significant under-prediction of the drag across the entire range of angles of attack for which data are given and exhibits approximate symmetry between negative and positive angles of attack, as expected from a simple box without skids.
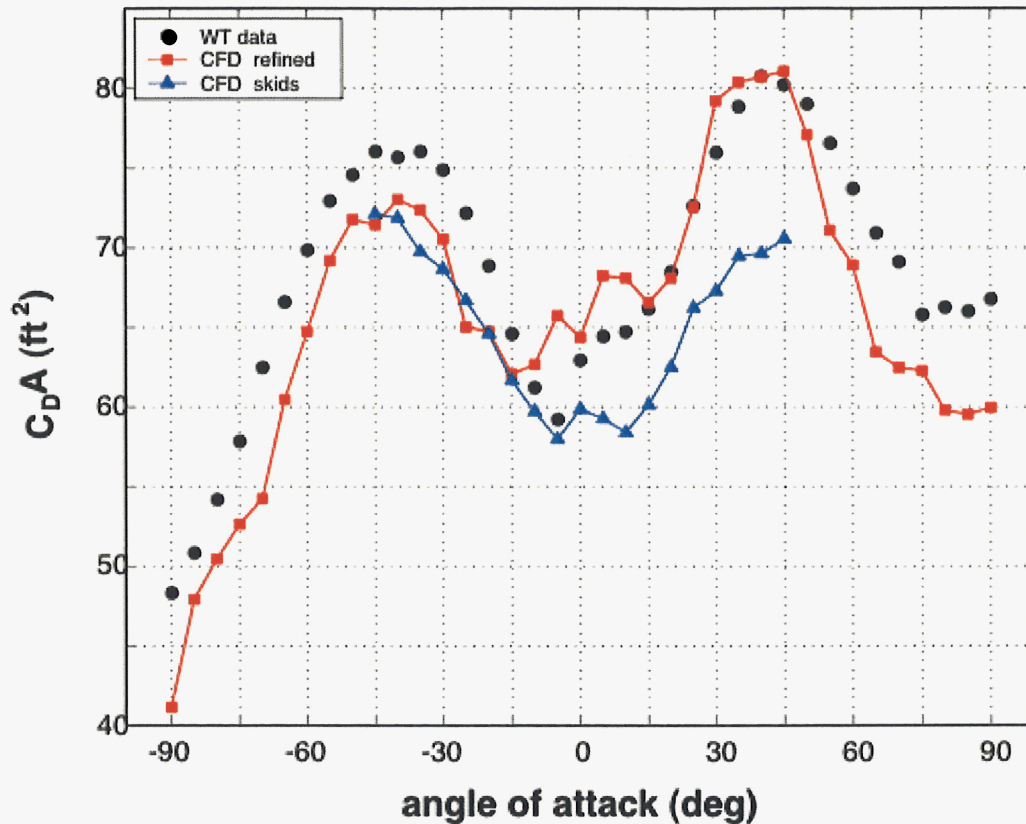


*Figure 17. Unsteady Flow Drag vs. Angle of attack – Compared to Wind Tunnel Data*

*Unsteady flow pitch moment vs. angle of attack*

Pitch moment data are shown below in Fig. 18. In the absence of skids, the pitching moment would be anti-symmetric about $\alpha = 0°$. The effects of the skids can be seen as departures from this anti-symmetry in the wind tunnel data. Strong effects occur for $|\alpha| < 40°$, up to 30 ft³. Simulation results for the **Original grid** (without skids) exhibit the expected anti-symmetry closely. The data for the grid with skids provide a closer fit to the wind tunnel data. It is especially accurate for most of the positive angle of attack range (skids facing into the wind) and less so at negative angles of attack (skids facing backwards). At zero degrees where an error bar is available, the CFD results do not accurately represent the wind tunnel data. The results do not give an insight as to the route to improvement of the CFD fit to the experimental data.

Possible routes are numerical factors (dissipation scheme, time step, turbulence model, etc) and an improved grid that includes the corrugations.

However the current dataset does not give insight to the possible route to improved CFD results; whether it is a numerical issue (dissipation scheme, time step size, turbulence model, etc.) or whether a grid that also includes the corrugations is required, is at this point only open to speculation.
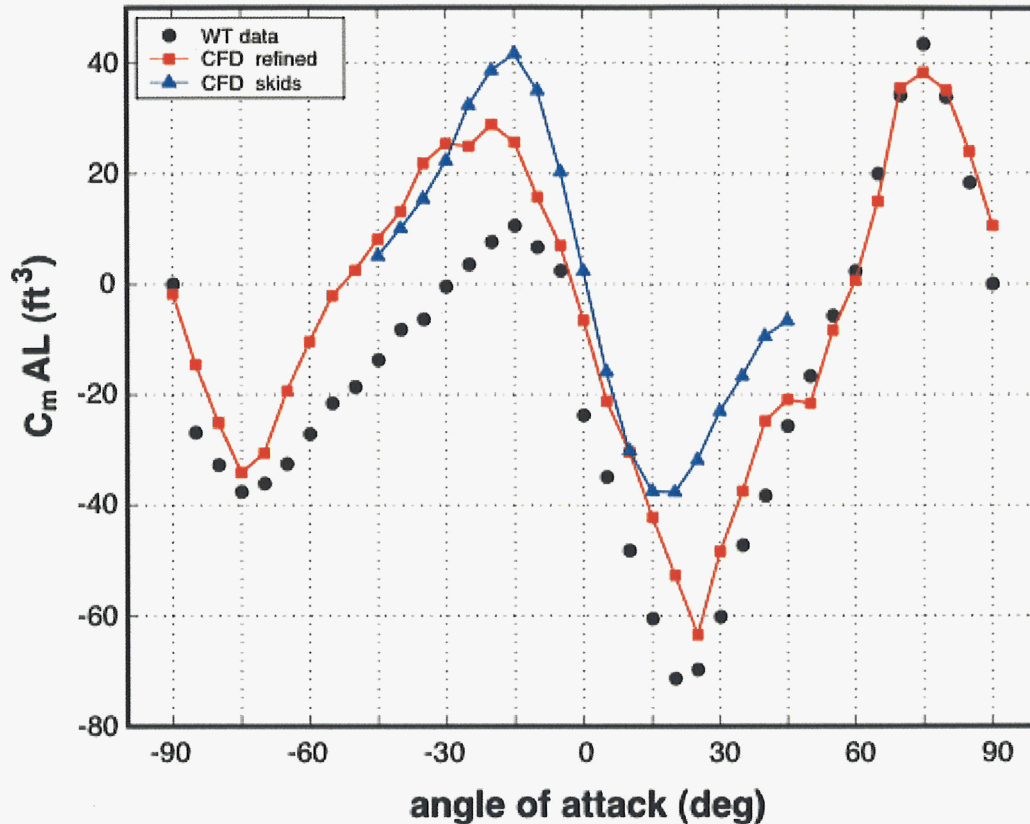


*Figure 18. UnsteadyFlow Pitch Moment vs. Angle of attack – Compared to Wind Tunnel Data*

*Unsteady flow lift vs. angle of attack*

Lift force data are presented in Fig. 19. The same comments made earlier with respect to data symmetry (and shown above in Fig. 17 and Fig. 18) also apply to the lift force. The **Refined grid** again under-predicts the lift force, but not by as large a margin as the pitching moment.

The grid with skids captures the negative peak at $\alpha = 15°$ with greater accuracy, but deviates significantly from wind tunnel data at more positive and more negative values of the angle of attack. At zero degrees, the wind tunnel data is well within the CFD error bar and the slope of the CLA-a curve in the vicinity of $\alpha = 0°$ is followed with great accuracy. In the region between 25° and 65° as well as –35° to –65° however, there is significant deviation between CFD results and wind tunnel data.
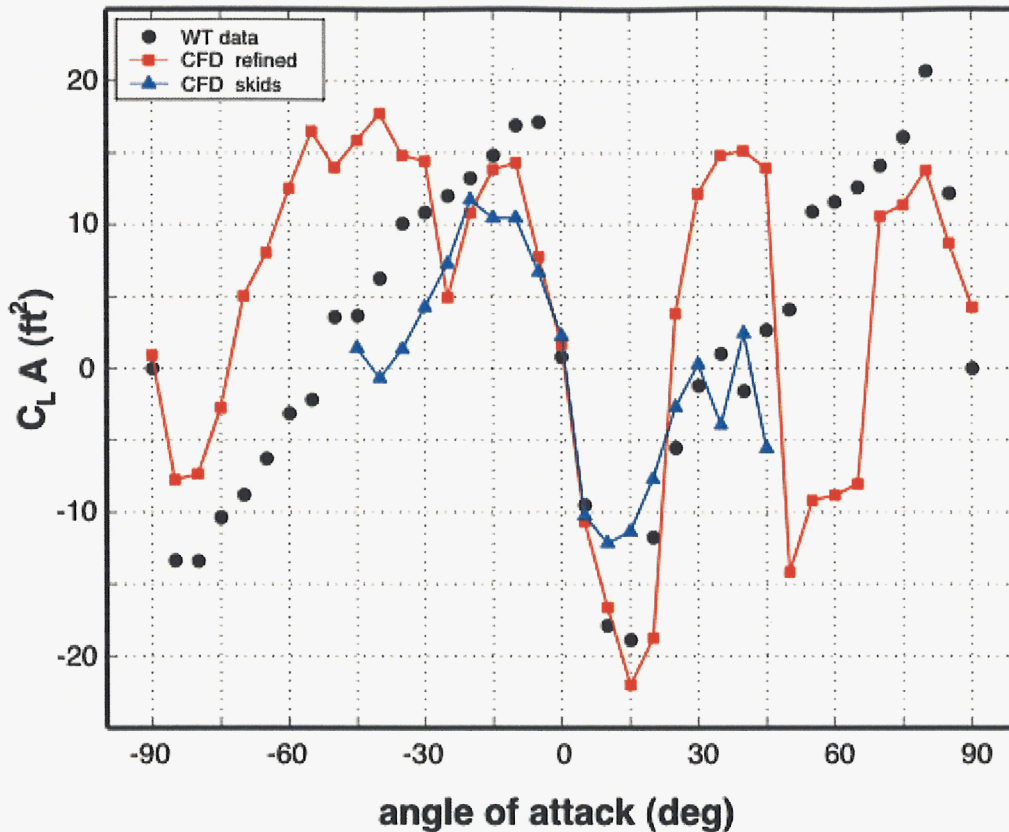
39

*Figure 19. Unsteady Flow Lift vs. Angle of Attack – Compared to Wind Tunnel Data*

The departures of the **Refined grid** data in Table 11b, Appendix E from the required symmetries of a box reflect numerical errors in the CFD calculations. Assuming these errors are random, a more probable value is obtained by averaging the data for a negative value of aoa with that for the positive value. The extreme departures from the average values are of size 2%, 12%, 6% for drag, lift and pitching moment, respectively, where percent is relative to the maximum values of the components in the wind tunnel data tables. Thus drag is accurate while lift shows large errors. A review of the data shows that the extreme errors are 2-sigma values.

### 3.3 Analysis of General Flow Features

The flow field in the midplane as viewed from above (+Z) is shown below as a function of sideslip angle in Figs. 20 to 29. The results presented are snapshots in time taken from the unsteady simulations. The freestream is flooded with velocity contours while the color on the body is $C_p$ (pressure coefficient). For both $C_p$ and velocity contours, low values are blue and high values indicated by red shading.

The red lines on the body are lines of surface-restricted flow generated by built-in functions of the FIELDVIEW visualization software [Ref. 22]. The presence of the lines indicates regions of flow separation and re-attachment. For the sake of brevity, only selected views from the +Z direction are included here. However, the view of the CONEX and the associated flow field from the –Y direction is included in Appendix I and further images from +Z in Appendix H.

*Figure 20. Flow field as Function of Side Slip Angle (0 Deg)*



*Figure 21. Flow Field as Function of Side Slip Angle (5 Deg)*

41

*Figure 22. Flow Field as a Function of Side Slip Angle (10 Deg)*



*Figure 23. Flow Field as a Function of Side Slip Angle (15 Deg)*

42

*Figure 24. Flow Field as Function of Side Slip Angle (20 Deg)*



*Figure 25. Flow Field as a Function of Side Slip Angle (35 Deg)*

*Figure 26. Flow Field as a Function of Side Slip Angle (45 Deg)*
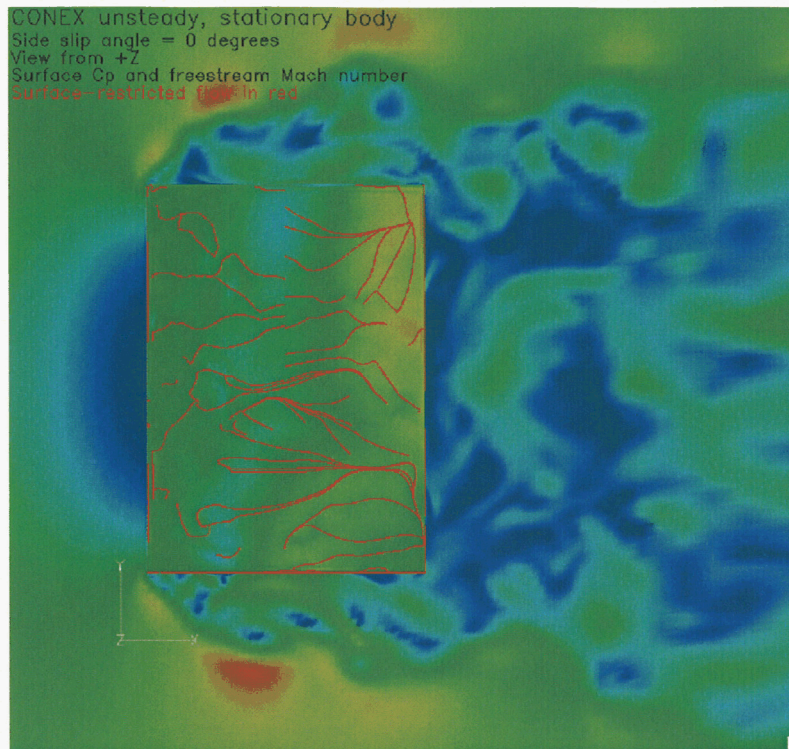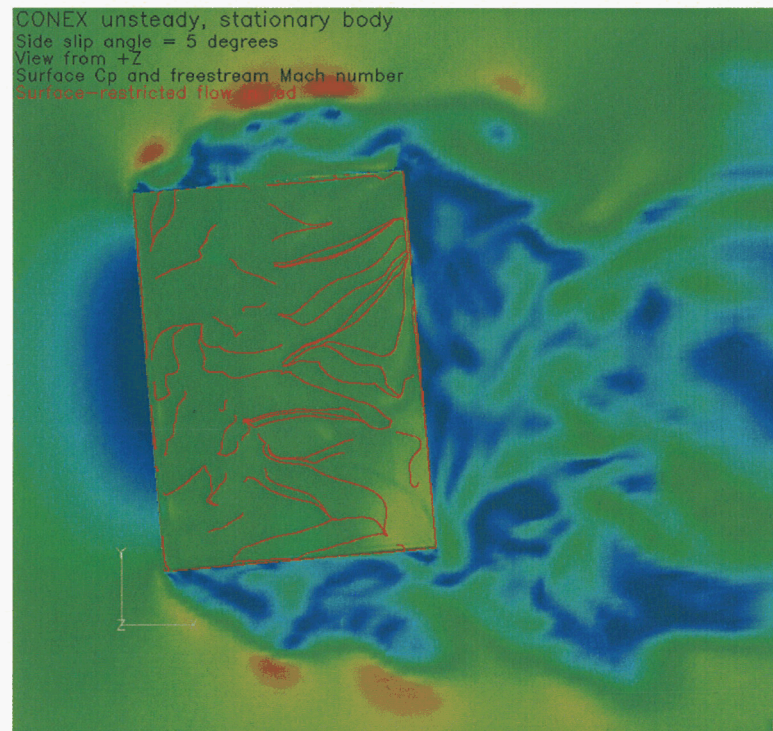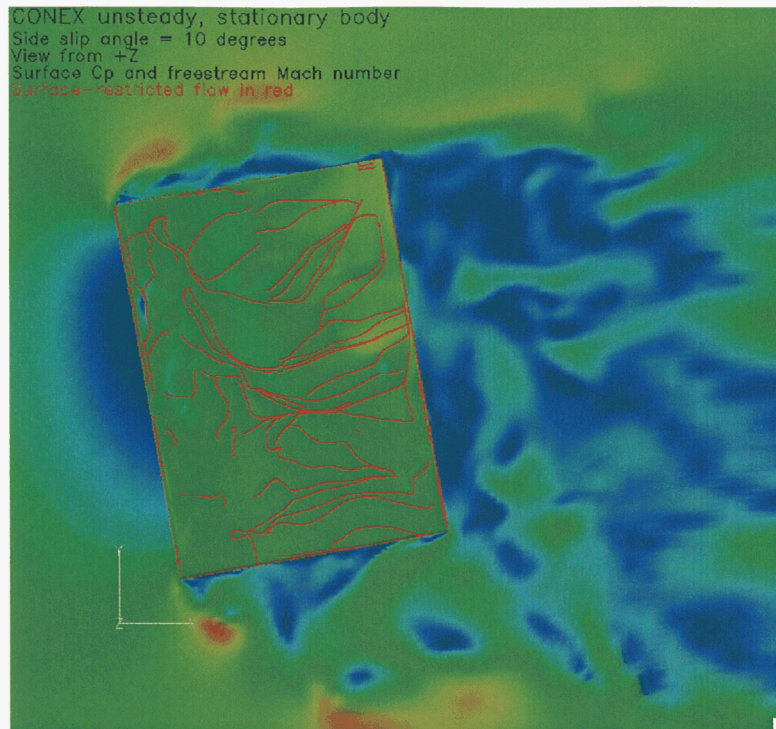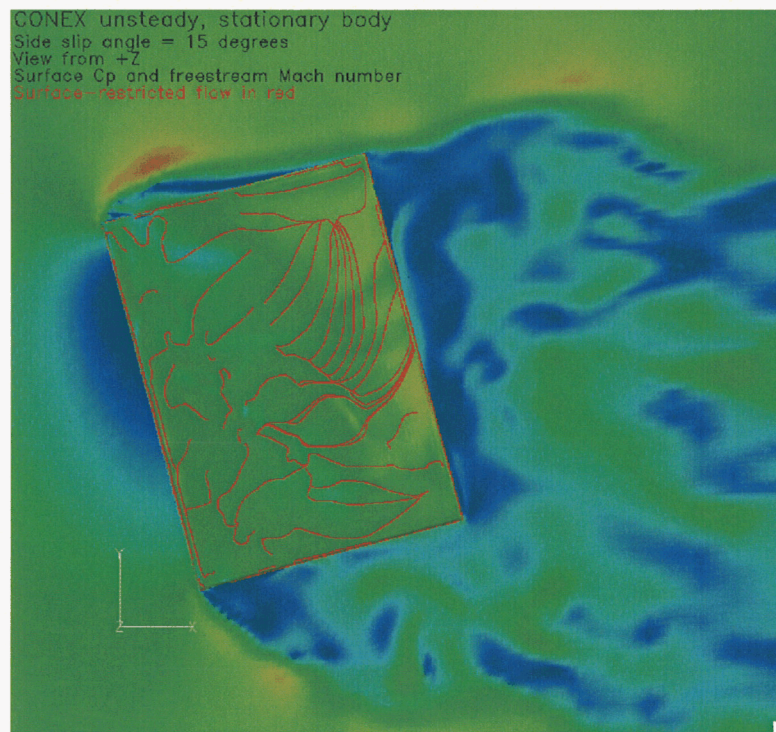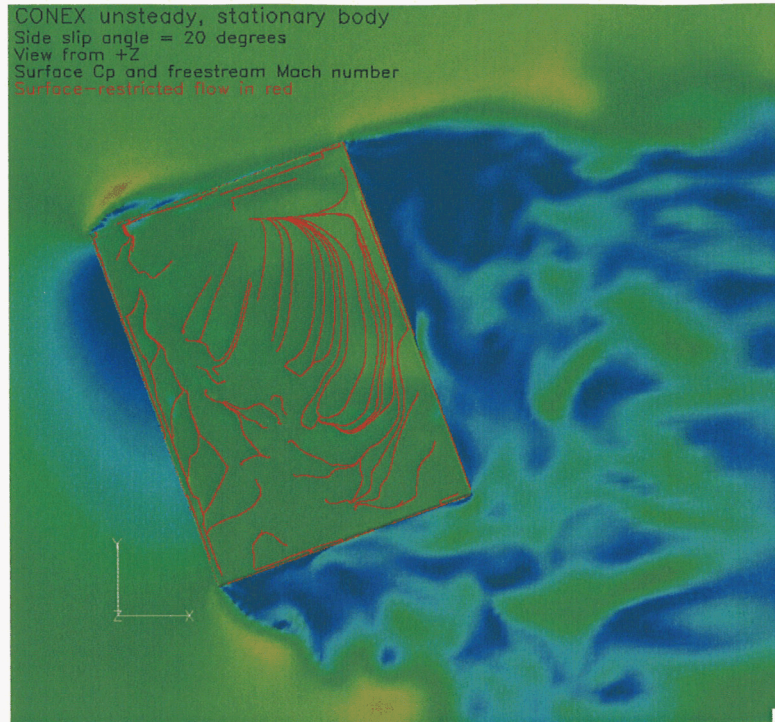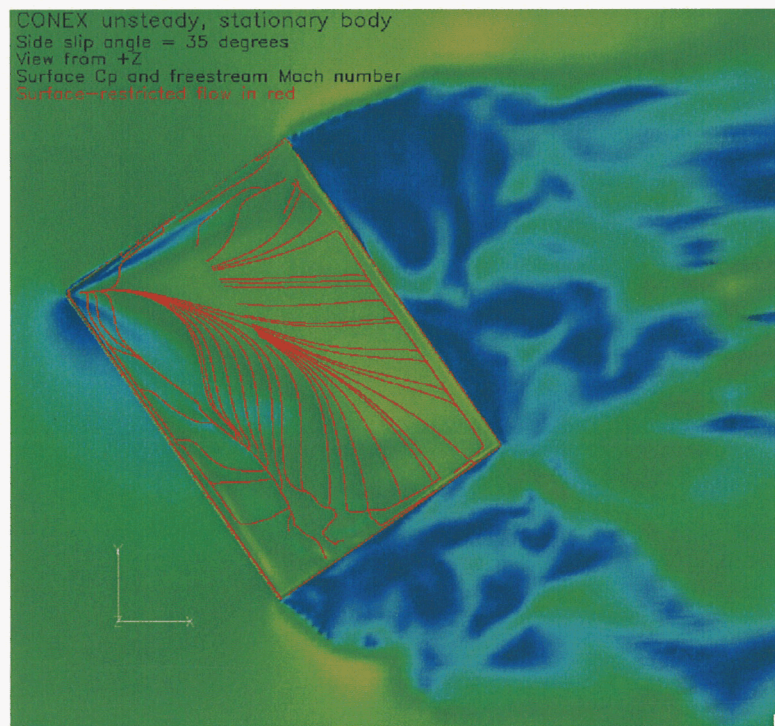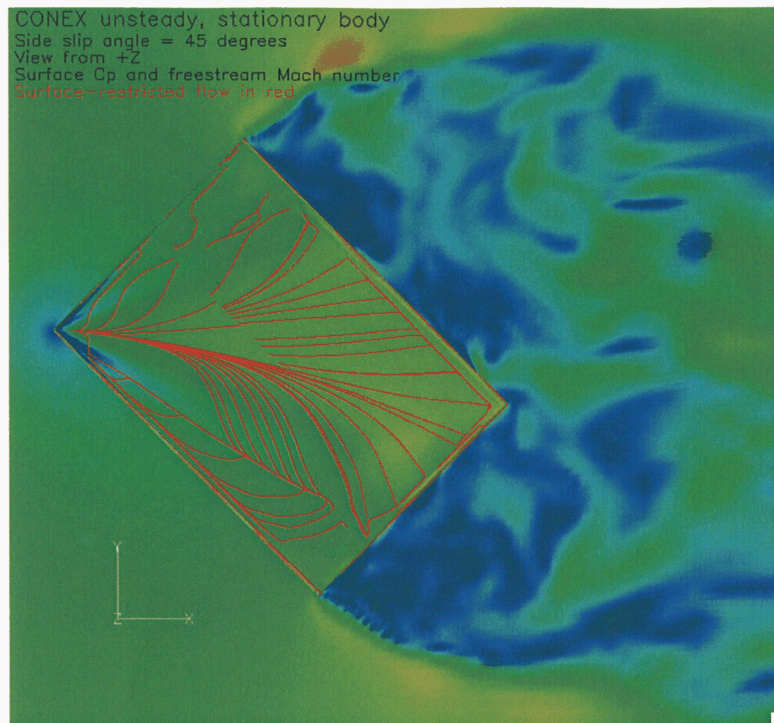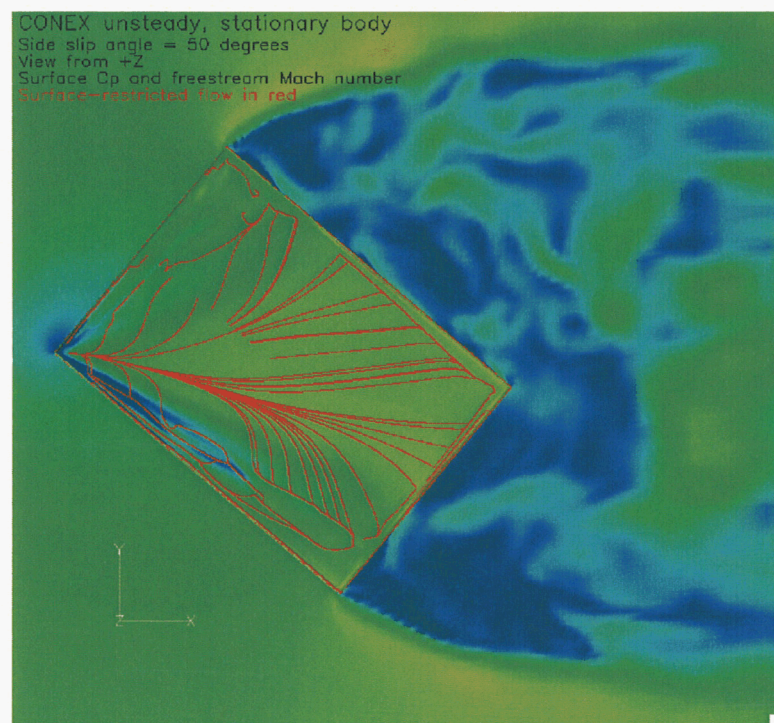


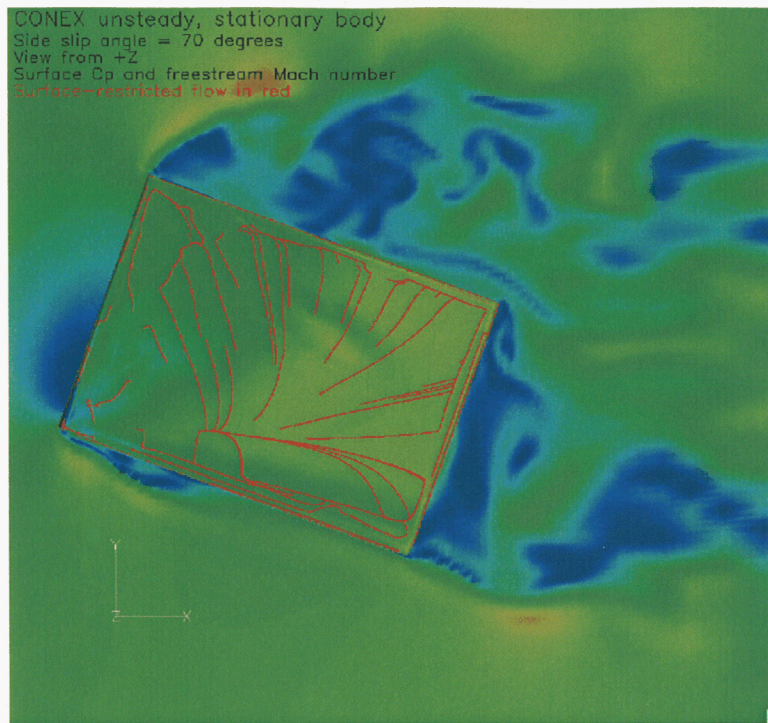*Figure 27. Flow Field as a Function of Side Slip Angle (50 Deg)*

*Figure 28. Flow Field as a Function of Side Slip Angle (70 Deg)*
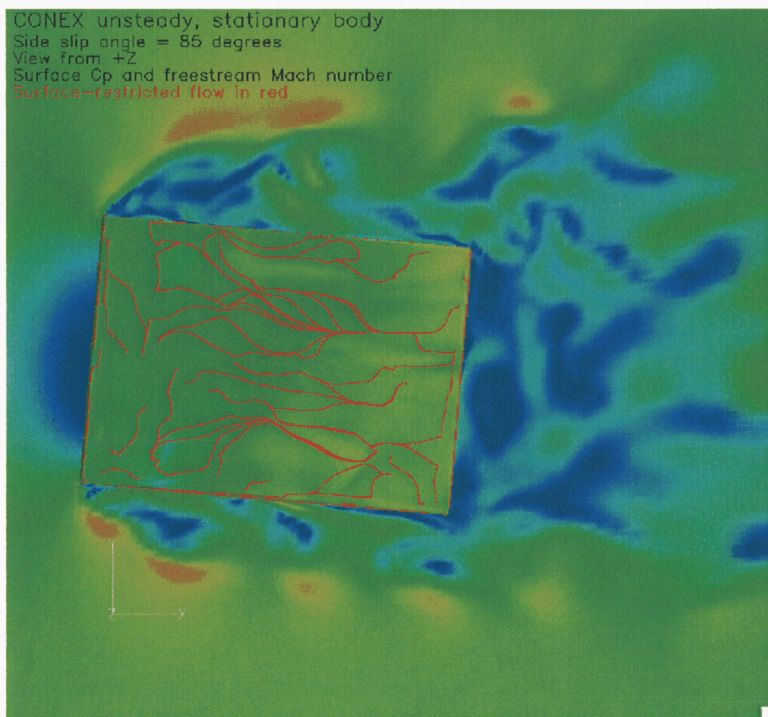


*Figure 29. Flow Field as a Function of Side Slip Angle (85 Deg)*

A number of features can be discerned from these figures. First, at angles of attack that place the leading face at angles approaching the perpendicular to the oncoming wind, there is massive separation from the two leading corners. This leads to an unstable shear layer with shed vortices buffeting the faces parallel to the wind. There is no noticeable structure on the upper and lower surfaces.

Second, when one of the faces is at small angles relative to the freestream, the unstable shear layer (a region where a high-velocity region meets a low velocity region and a distinct line is formed as indicated in Fig. 23) becomes more stable and the separated flow re-attaches. This leads to a recirculating region and an unstable separation bubble (the upper face at 15° in Fig. 23 and the lower face at 70° in Fig. 28) that bursts periodically and sheds downstream (see Fig. 30 below). This separation bubble shrinks and becomes more stable as the sideslip angle increases.

Third, the appearance of this stable but very small separation bubble (side slip angle between 35° and 50°) coincides with the formation of two counter-rotating vortices on the upper and lower surfaces as indicated by the diagonal red separation and re-attachment lines. The presence of the counter-rotating vortices can also be discerned by the presence of blue (low values) regions of the pressure coefficient emanating from the corner facing the wind and sweeping back on the top and bottom faces along the edges facing the wind (as seen in Figs. 25 to 27).

As the sideslip angle is further increased, the process reverses itself; the separation bubble grows and becomes less stable (while the counter-rotating vortices break up), and the bubble eventually transitions into fully separated flow.

The flow patterns shown above also give some insight into the maximum drag value observed in the wind tunnel at 40° to 45° side slip angle (see Fig. 7). For both sideslip angles of 35° and 50°, the shear layers emanating from the two corners of the CONEX not in a stagnation position or hidden behind the CONEX, are stable. Furthermore, there are no unstable separation bubbles on the faces directly exposed to the wind, leading to high friction drag values. These (35° and 50°) are also the sideslip angles where there is a stable, counter-rotating vortex on the top face (facing the viewer and indicated by red-colored, coherent separation and re-attachment lines).

Taking these observations into account one may conclude that less drag is produced by a bluff body subject to massive separation than the same body in a flow field that is characterized by stable vortical structures and coherent, stable shear layers.
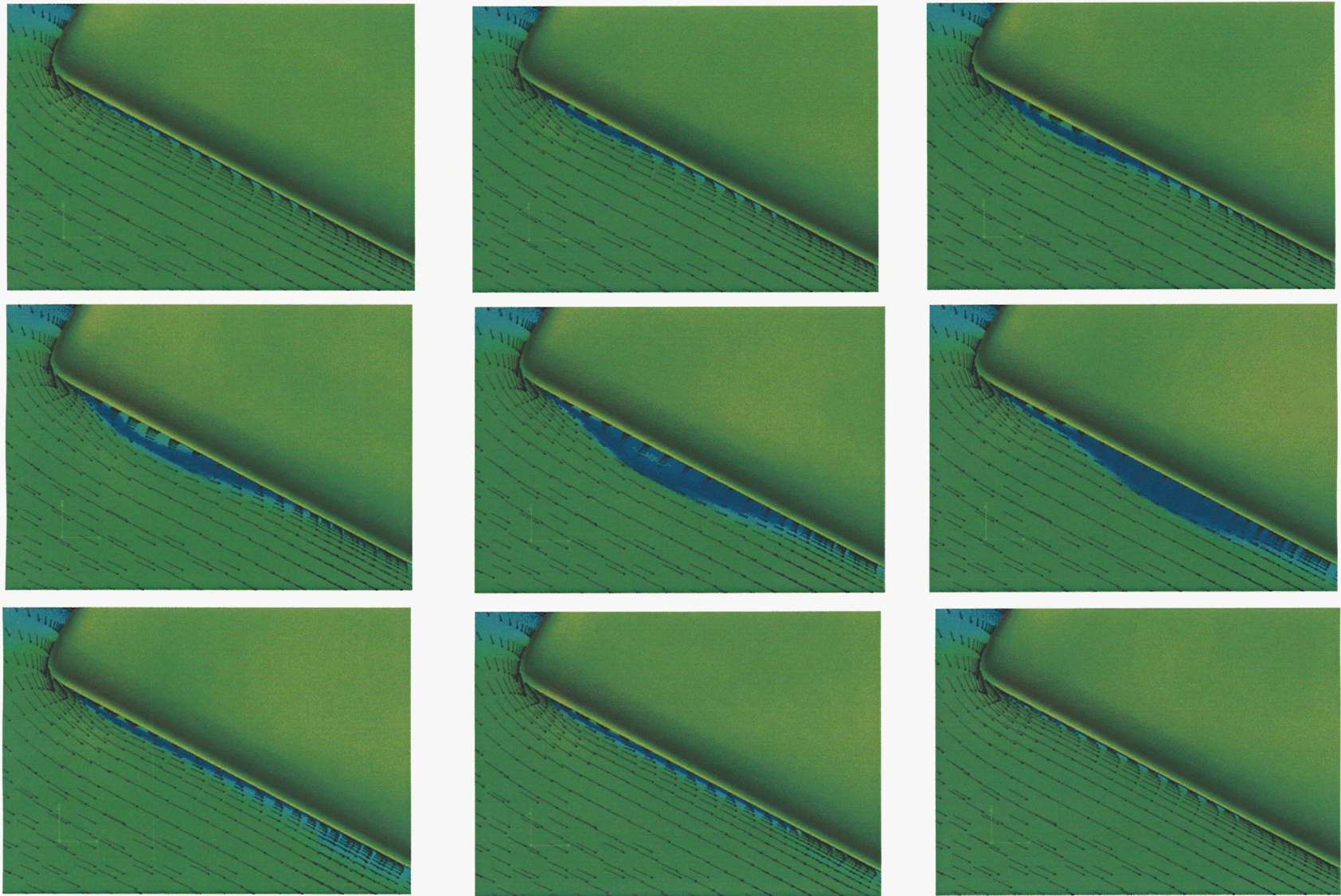
Figure 30. Time Sequence of Separation Bubble Shedding from the Bottom Face at 60 Deg Side Slip Angle

# 4.CONCLUSIONS

The following conclusions can be drawn:

1. The effect of the turbulence model was studied using a simplified grid in steady-state mode. From these results it is clear that the Baldwin-Barth model compared best to wind tunnel data.
2. Data were shown to be invariant with Machnumber out to 0.3 Mach number. A previous two-dimensional CFD study showed invariance with Reynolds number over the range of interest for the tunnel model scale and full-scale container. That work has not been expanded upon here.
3. In a time-averaged unsteady DES-SA analysis of flow about the CONEX, CFD accurately predicts i) drag force and yaw moment vs. side slip angle (b) and ii) drag force and pitching moment vs. angle of attack (a). Side force vs. b and lift force vs. angle of attack (a) are less accurately predicted by CFD.
4. Not surprisingly, the CFD grid that included a representation of the skids approximated the wind tunnel data more closely than grids that model the basic box-like geometry. There are unanswered questions regarding the effect of skids on forces and moments as a function of side slip angle. The magnitude of the effect of skids on some forces (for example drag force as a function of angle of attack) were surprisingly large.
5. High drag values are associated with stable shear layers off the body, small or negligible separation bubbles and attached vortices on the body. Low drag appears to be associated with unstable shear layers and the presence of unstable separation bubbles.
6. Using 6 million grid points to represent the CONEX with skids and the steady flow Navier-Stokes equations, and 16 nodes on a fast HPC cluster, a complete table of static aerodynamics (every 5 deg in angle of attack over [-90,90] and in beta over [0,180], would require 252 days. This is reduced to 57 days on the Columbia super computer and can be further reduced by running multiple cases simultaneously, depending on the number of nodes available.

An unsteady CFD solver based on OVERFLOW has been applied to simulate the massively separated chaotic flow around a rectangular cargo container and validated against wind tunnel data for the stationary box with a substantial degree of success.

# REFERENCES

1. Tyson, P., "Simulation Validation and Flight Prediction of UH-60A Black Hawk Helicopters/Slung Load Characteristics," M.Sc. Thesis, Naval Postgraduate School, U.S. Naval Academy, March 1999.

2. Cicolani, L. S., da Silva, J. G. A., Duque, E. P. N., and Tischler, M., "Unsteady Aerodynamic Model of a Cargo Container for Slung-Load Simulation: Preliminary Aerodynamic Data and Model Identification," NASA/TP-2004-212817, May 2004.

3. Cicolani, L. S., McCoy, A. H., Sahai, A. H., Tyson, R., Tischler, M. .B., Ronen, A., and Tucker, G., "Flight Test Identification and Simulation of a UH-60A Helicopter and Slung Load", *Journ. American Helicopter Society*, 46, pp. 140-160, 2001.

4. Theron, J. N., Duque, E. P. N., Cicolani, L. and Halsey, R., "3D CFD Simulation of a Spinning Helicopter Slung Load", presented at the 31st European Rotorcraft Forum, Florence, Italy, September 13-15 2005.

5. L. S. Cicolani, J. G. A. da Silva, E. P. N. Duque and M. B. Tischler, "Unsteady Aerodynamic Model of a Cargo Container for Slung-Load Simulation", *The Aeronautical Journal*, p. 357, July, 2004.

6. Rosen, A., Cecutta, S. and Yaffe, R.: "Wind Tunnel Tests of Cube and CONEX Models," Technion - Institute of Technology, Faculty of Aerospace Engineering TAE 844, November, 1999.

7. McCormick, B. W. , Jr., *Aerodynamics of V/STOL Flight*, p. 31, Dover Publications, Inc., 1999, Mineola, NY (first published in 1967).

8. Buning, P. G., Chiu, I. T., Obayashi, S., Rizk, Y. M. and Steger, J. L., "Numerical Simulation of the Integrated Space Shuttle Vehicle in Ascent", AIAA 88-4359, AIAA Atmospheric Flight Mechanics Meeting, Minneapolis, MN, August 15-17, 1988.

9. Buning, P. G. Jespersen, D. C., Pulliam, T. H., Klopfer, G. H., Chan, W. M., Slotnick, J. P., Krist, S. E. and Renze, K. J., OVERFLOW Users Manual Version 1.8aa, 24 April 2003.

10. Ahmad, J. and Duque, E. P. N., "Helicopter Rotor Blade Computation in Unsteady Flows Using Moving Overset Grids," *Journal of Aircraft*, Vol. 33, No. 1, pp. 54-60, January-February 1996.

11. Meakin, R., "Moving Grid Overset Grid Methods for Complete Aircraft Tiltrotor Simulations," AIAA Paper 93-3350, July 1993.

12. Pulliam, T.H. and Steger, J.L., "Implicit Finite-Different Simulations of Three-Dimensional Compressible Flow", *AIAA Journal* Vol. 18, No. 2, p. 159, February 1980.

13. Anderson, J. D., *Computational Fluid Dynamics: The Basics with Application*, McGraw-Hill, New York (1995).

14. Baldwin, B. S. and Barth, T. J., "A One-Equation Turbulence Transport Model for High Reynolds Number Wall-Bounded Flows," NASA TM 102847, August 1990.

15. Spalart P. R., Allmaras S. R., "A One-equation Turbulence Model for Aerodynamic Flows," 29th Aerospace Sciences Meeting, Reno, NV, AIAA-92-0439, January 1992.

16. Menter, F. R. "Two-equation Eddy-Viscosity Turbulence Models for Engineering Applications," *AIAA Journal* Vol. 32 No. 8, pp. 598-605,1994.

17. Strelets M., "Detached Eddy Simulation of Massively Separated Flows," 39th Aerospace Sciences Meeting and Exhibit, Reno, NV 2001, AIAA Paper 2001-0879.

18. Personal communication, Philippe Spalart, January 31, 2005.

19. Chan, W. M., "The OVERGRID Interface for Computational Simulations on OVERSET Grids", 32nd AIAA Fluid Dynamics Conference, St.Louis Missouri, AIAA-2002-3188, June 2002.

20. Chan, W. M. and Buning, P. G., Users Manual for FOMOCO Utilities - Force and Moment Computation Tools for Overset Grids , NASA TM 110408, July 1996.

21. Personal communication, Suresh Menon, Georgia Institute of Technology, 2005.

22. FIELDVIEW, Visualization software by Intelligent Light (www.ilight.com).

## APPENDIX A    NONDIMENSIONAL CALCULATIONS FOR OVERFLOW

The Navier-Stokes equations are used in nondimensional form internal to OVERFLOW [Ref. 9]. Consequently the solver inputs also have to be nondimensionalized. The fluid is air at 68° with kinematic viscosity of 1.61E-4 ft²/sec.

Time (t) is nondimensionalized according to the definition in Equation 7  where $a_\infty$ is the speed of sound in the freestream and L is a reference length). At sea level, the speed of sound in air is 1,116.47 ft/sec and the reference length is chosen as 6.11ft.

$$t^* = \frac{t\, a_\infty}{L} = \frac{1,116.47\,\text{ft/sec}}{6.11\,\text{ft}}t = 182.728t \qquad (7)$$

The Reynolds number (based on the short side length of the CONEX and calculated at 60kts) is

$$Re = \frac{U.L}{\upsilon} = \frac{101.628\,\text{ft/sec} \times 6.11\,\text{ft}}{1.61\text{E-4}\,\text{ft}^2/\text{sec}} = 3,856,814 \qquad (8)$$

However, Reynolds number has to be expressed per unit body length for proper OVERFLOW input:

$$Re^* = \frac{Re}{L} = \frac{3,856,814}{6.11\,\text{ft}} = 631,230\ \text{ft}^{-1} \qquad (9)$$

At a forward velocity of 60 knots the Mach number (M) is:

$$M = \frac{U}{a_\infty} = \frac{101.628\,\text{ft/sec}}{1,116.47\,\text{ft/sec}} = 0.091 \qquad (10)$$

## APPENDIX B    OVERFLOW INPUT FILES

Fixed attitude and prescribed motion is generated using the xml files. Config.xml defines the grouping of the grids into components and controls the original transformation of grids while Scenario.xml defines the motion of these bodies.  For fixed attitude cases the Scenario files are not used.

**Config.xml:**

```
<?xml version='1.0' encoding='utf-8'?>
<Configuration AngleUnit="degree">

  <Component Name="COMP 1" Type="struc">
    <Data> Grid List=1-3 </Data>
    <Transform>
     <Rotate Center="0.0, 0.0, 0.0" Axis="0.0, 0.0, 1.0" Angle="10.0" />
    </Transform>
  </Component>

 </Configuration>
```

**Scenario.xml:**

```
<?xml version='1.0' encoding='utf-8'?>
<Scenario AngleUnit="degree">

<Prescribed Component="COMP 1" Start="0" Duration="9999.9" >
  <Rotate Center="0.0, 0.0, 0.0" Axis="0.0, 0.0, 1.0" Speed="0.0" Frame="parent" />
</Prescribed>

</Scenario>
```

In the above case, the CONEX (consisting of grids 1-3) is held in a stationary position with the broad side at a sideslip angle of $10°$ to the wind.  The right hand rule is used to rotate the body about the upward-pointing Z axis.

**OVERFLOW input file**

In the case listed below, the DES-SA turbulence model was selected (NQT=104). This model offers accuracy comparable to more-complex and computationally-intensive two-equation models such as k-e and k-w. Initial runs showed that the simulation was unstable, so CFLMAX values of 20.0 were incorporated in the input file to effectively control the time step size in localized regions. Second-order dissipation terms were set to zero (DIS2=0.0 – no shock present) and fourth-order dissipation terms (DIS4) were set at 0.01 for accuracy in skin friction calculations. All viscous terms were turned off, except for the near-body grids in the L direction (pointing perpendicular away from the surface). Second-order central spatial discretization (FSO

= 2.0) and first-order time-accuracy (TFOSO=1.0) was used. The example OVERFLOW input file given below was for the Refined grid (consisting of three near-body grids).

```
$GLOBAL
  RESTRT  = .F.,
  NSTEPS  = 30000,
  NFOMO   = 5,
  NSAVE   = -2000,
  NQT     = 104,
  DTPHYS  = 0.01, !0.1 deg/s
  !NITNWT = 5,
  !FSONWT = 1,
  $END

$OMIGLB
  IRUN = 0,
  LFRINGE = 1,
  DYNMCS = .F.,
  I6DOF = 2,
  NADAPT = 0,
  SIGERR = 2.0,
  IBXMIN = 47,
  IBXMAX = 47,
  IBYMIN = 47,
  IBYMAX = 47,
  IBZMIN = 47,
  IBZMAX = 47,
  $END

$DCFGLB
  DQUAL = 1.0,  MORFAN = 1,  NORFAN = 5,
  $END

$GBRICK
  OBGRIDS = .T.,
  DFAR = 90,  DS = 0.125,  CHRLEN = 6.11,
  XNCEN = 0,  YNCEN = 0,  ZNCEN = 0,
  $END

$BRKINP
  NBRICK  =  -1,
  XBRKMIN = -6.0,
  XBRKMAX =  12.0,
  YBRKMIN = -6.0,
  YBRKMAX =  6.0,
  ZBRKMIN = -4.5,
```

```
    ZBRKMAX =  4.5,
    IBDYTAG =    0,
    $END

$GROUPS
  USEFLE = .T.,
  IGSIZE = 3000000, MAXNB = 100000,  MAXGRD = 40000,
  WGHTNB = 1.8,
    $END

$XRINFO
  IDXRAY = 1, IGXLIST = -1, XDELTA = 0.35,
    $END

$FLOINP
  FSMACH = 0.0907059,
  ALPHA  = 0.0,
  BETA   = 0.0,
  REY    = 632100,
  TINF   = 518.67,
  GAMINF = 1.4,
    $END

$VARGAM $END


$GRDNAM
  NAME = 'GRID_1',
    $END

$NITERS $END

$METPRM
  IRHS = 0,  ILHS = 2,  IDISS = 4,
  BIMIN = -1.0,
    $END

$TIMACU
  ITIME = 0, CFLMAX = 20.0, TFOSO = 1.0,
    $END

$SMOACU
  SMOO = 0.0, DIS2 = 0.0, DIS4 = 0.04,
  FSO = 2.0,
    $END
```

```
$VISINP
  VISCJ = .F., VISCK = .F., VISCL = .T.,
  $END

$BCINP
  NBC = 2,
  IBTYP =   5,  10,
  IBDIR =   3,   1,
  JBCS  =   1,   1,
  JBCE  =  -1,   1,
  KBCS  =   1,   1,
  KBCE  =  -1,  -1,
  LBCS  =   1,   1,
  LBCE  =   1,  -1,
  $END

$SCEINP $END
$SIXINP $END

$GRDNAM
  NAME = 'GRID_2',
  $END

$NITERS $END

$METPRM
  IRHS = 0,  ILHS = 2,  IDISS = 4,
  BIMIN = -1.0,
  $END

$TIMACU
  ITIME = 0, CFLMAX = 20.0, TFOSO = 1.0,
  $END

$SMOACU
  SMOO = 0.0, DIS2 = 0.0, DIS4 = 0.01,
  FSO = 2.0,
  $END

$VISINP
  VISCJ = .F., VISCK = .F., VISCL = .T.,
  $END

$BCINP
  NBC = 1,
  IBTYP =   5,
```

```
      IBDIR =    3,
      JBCS  =    1,
      JBCE  =   -1,
      KBCS  =    1,
      KBCE  =   -1,
      LBCS  =    1,
      LBCE  =    1,
      $END

$SCEINP $END
$SIXINP $END

$GRDNAM
   NAME = 'GRID_3',
   $END

 $NITERS $END

 $METPRM
   IRHS = 0,  ILHS = 2,  IDISS = 4,
   BIMIN = -1.0,    $END

 $TIMACU
   ITIME = 0, CFLMAX = 20.0, TFOSO = 1.0,
   $END

 $SMOACU
   SMOO = 0.0, DIS2 = 0.0, DIS4 = 0.01,
   FSO = 2.0,    $END

 $VISINP
   VISCJ = .F., VISCK = .F., VISCL = .T.,
   $END

 $BCINP
   NBC = 1,
   IBTYP =    5,
   IBDIR =    3,
   JBCS  =    1,
   JBCE  =   -1,
   KBCS  =    1,
   KBCE  =   -1,
   LBCS  =    1,
   LBCE  =    1,
   $END
```

```
$SCEINP $END
$SIXINP $END

$GRDNAM
  NAME = 'Off-body grids',
   $END

$NITERS $END
$METPRM $END

$TIMACU
  ITIME = 0, CFLMAX = 0., TFOSO = 1.0,
   $END

$SMOACU
  SMOO = 0.0, DIS2 = 0.0, DIS4 = 0.01,
  FSO = 2.0,     $END

$VISINP
  VISC = .T.,
   $END

$BCINP   $END
$SCEINP $END
```

# APPENDIX C   STEADY-STATE DATA, SIDESLIP ANGLE, ORIGINAL GRID

**Table 6: Steady-State CFD Results Using the Baldwin-Barth
Turbulence Model – Sideslip Angle**

| Sideslip angle deg | Drag force $ft^2$ | Side force $ft^2$ | Yaw moment $ft^3$ |
|---|---|---|---|
| | $C_DA$ | $C_YA$ | $C_nAL$ |
| 0 | 65.96 | 0.46 | 0.12 |
| 5 | 64.80 | 8.92 | 9.74 |
| 10 | 64.46 | 15.79 | 24.53 |
| 15 | 63.14 | 16.56 | 34.29 |
| 20 | 65.18 | 16.46 | 36.67 |
| 30 | 62.96 | 14.60 | 26.68 |
| 40 | 61.74 | 15.87 | 20.72 |
| 45 | 58.53 | 13.91 | 16.50 |
| 55 | 55.59 | 10.95 | 3.41 |
| 60 | 52.51 | 8.81 | -2.76 |
| 75 | 44.76 | 4.31 | -29.73 |
| 80 | 42.21 | 0.52 | -35.97 |
| 85 | 40.08 | -3.00 | -27.64 |
| 90 | 40.92 | -0.28 | -0.62 |

**Table 7. Steady-State CFD Results Using the Spalart-Allmaras
Turbulence Model
– Sideslip Angle**

| Sideslip angle deg | Drag force ft$^2$ | Side force ft$^2$ | Yaw moment ft$^3$ |
|---|---|---|---|
| | $C_DA$ | $C_YA$ | $C_nAL$ |
| 0 | 59.44 | -0.17 | 0.98 |
| 5 | 59.34 | 9.20 | 11.83 |
| 10 | 60.12 | 13.88 | 29.98 |
| 15 | 61.36 | 16.51 | 42.46 |
| 20 | 64.55 | 14.82 | 41.76 |
| 30 | 65.30 | 15.89 | 29.31 |
| 40 | 63.35 | 15.92 | 22.00 |
| 45 | 60.86 | 14.27 | 17.27 |
| 55 | 57.07 | 8.44 | 3.02 |
| 60 | 53.15 | 2.73 | -2.84 |
| 65 | 51.17 | 5.27 | -11.72 |
| 75 | 44.93 | 4.10 | -30.27 |
| 80 | 40.83 | 1.99 | -33.33 |
| 85 | 38.84 | -1.80 | -27.87 |
| 90 | 37.49 | -0.03 | 0.15 |

**Table 8: Steady-State CFD Results Using the Kω Turbulence Model – Sideslip Angle**

| Sideslip angle deg | Drag force $ft^2$ | Side force $ft^2$ | Yaw moment $ft^3$ |
|---|---|---|---|
| | $C_DA$ | $C_YA$ | $C_nAL$ |
| 0 | 52.68 | -0.21 | -0.27 |
| 5 | 54.92 | 8.81 | 24.57 |
| 10 | 55.39 | 9.85 | 35.28 |
| 15 | 61.35 | 12.95 | 42.99 |
| 20 | 62.26 | 12.72 | 36.73 |
| 30 | 64.66 | 18.53 | 20.32 |
| 40 | 62.32 | 16.87 | 11.38 |
| 45 | 61.18 | 14.89 | 16.62 |
| 55 | 56.06 | 2.26 | 12.15 |
| 60 | 54.55 | 1.55 | 3.95 |
| 75 | 45.07 | 7.02 | -20.56 |
| 80 | 40.77 | 6.04 | -20.19 |
| 85 | 36.24 | 2.26 | -15.57 |
| 90 | 33.28 | 0.07 | 0.11 |

**Table 9: Steady-State CFD Results Using the Kω-SST Turbulence Model – Sideslip Angle**

| Sideslip angle deg | Drag force ft$^2$ | Side force ft$^2$ | Yaw moment ft$^3$ |
|---|---|---|---|
| | $C_DA$ | $C_YA$ | $C_nAL$ |
| 0 | 55.84 | 0.46 | 3.05 |
| 5 | 57.73 | 9.03 | 14.85 |
| 10 | 56.90 | 15.42 | 31.85 |
| 15 | 59.93 | 16.46 | 49.49 |
| 20 | 62.60 | 14.97 | 50.07 |
| 30 | 65.15 | 18.67 | 26.88 |
| 40 | 63.11 | 16.44 | 15.07 |
| 45 | 61.17 | 15.00 | 8.96 |
| 55 | 55.98 | 4.90 | 6.16 |
| 60 | 54.37 | 0.13 | 0.55 |
| 75 | 44.93 | 4.77 | -27.67 |
| 80 | 40.38 | 3.07 | -27.30 |
| 85 | 36.49 | -2.84 | -22.34 |
| 90 | 35.65 | 0.73 | 0.79 |

# APPENDIX D     UNSTEADY FLOW DATA, SIDESLIP ANGLE, REFINED GRID

**Table 10.  Unsteady Flow CFD Results Using the DES-SA Turbulence Model – Sideslip Angle, Refined Grid**

| Sideslip angle deg | MOMENTS ft$^3$ | | | FORCES ft$^2$ | | |
|---|---|---|---|---|---|---|
| | Yaw $C_nAL$ | Pitch $C_mAL$ | Roll $C_lAL$ | Lift $C_LA$ | Drag $C_DA$ | Side $C_YA$ |
| 0 | 0.20 | -0.14 | -0.02 | 0.06 | 62.83 | -0.02 |
| 5 | 14.97 | 2.28 | 0.40 | 1.25 | 58.92 | 5.32 |
| 10 | 31.74 | 1.17 | -0.84 | 1.21 | 59.11 | 8.84 |
| 15 | 38.24 | 0.90 | 0.19 | 0.10 | 60.64 | 9.59 |
| 20 | 35.49 | 1.27 | 0.29 | -0.46 | 62.56 | 10.68 |
| 25 | 30.56 | -0.85 | 2.06 | -0.78 | 64.29 | 10.89 |
| 30 | 26.69 | 0.17 | 0.30 | -0.28 | 64.26 | 11.42 |
| 35 | 20.57 | 2.05 | -0.69 | 0.28 | 63.10 | 10.33 |
| 40 | 17.79 | -1.20 | 0.05 | -0.56 | 62.86 | 13.56 |
| 45 | 12.87 | -0.76 | 0.13 | -0.01 | 61.90 | 12.70 |
| 50 | 8.14 | 0.76 | 0.33 | 0.43 | 60.15 | 14.95 |
| 55 | 1.91 | -0.09 | 0.58 | -0.14 | 58.34 | 14.63 |
| 60 | -4.64 | 1.56 | -1.00 | 0.45 | 55.08 | 13.55 |
| 65 | -13.93 | -1.85 | 1.05 | -0.25 | 52.34 | 12.05 |
| 70 | -23.29 | 0.22 | 1.41 | -0.48 | 49.18 | 13.21 |
| 75 | -35.75 | 1.77 | -0.64 | 0.22 | 45.82 | 9.49 |
| 85 | -27.18 | -3.13 | 0.46 | 0.34 | 38.19 | 5.43 |
| 90 | -1.43 | 1.48 | 0.89 | -0.77 | 36.13 | -0.22 |

# APPENDIX E  UNSTEADY DATA, ANGLE OF ATTACK, GRID WITH SKIDS

**Table 11a.  Unsteady Flow CFD Results Using the DES-SA Turbulence Model –Angle of Attack, Grid with Skids**

| Angle of Attack deg | Force Coefficients ft$^2$ | | Pitching moment ft$^3$ |
|---|---|---|---|
| | $C_DA$ | $C_LA$ | $C_mAL$ |
| -90 | 41.16 | 0.92 | -1.81 |
| -85 | 47.93 | -7.74 | -14.58 |
| -80 | 50.46 | -7.34 | -25.10 |
| -75 | 52.65 | -2.73 | -34.10 |
| -70 | 54.24 | 5.04 | -30.56 |
| -65 | 60.47 | 8.05 | -19.34 |
| -60 | 64.73 | 12.53 | -10.46 |
| -55 | 69.18 | 16.52 | -2.13 |
| -50 | 71.77 | 14.00 | 2.46 |
| -45 | 71.43 | 15.90 | 8.11 |
| -40 | 73.01 | 17.76 | 13.10 |
| -35 | 72.37 | 14.83 | 21.84 |
| -30 | 70.52 | 14.42 | 25.41 |
| -25 | 65.00 | 4.94 | 24.91 |
| -20 | 64.73 | 10.81 | 28.90 |
| -15 | 62.05 | 13.84 | 25.65 |
| -10 | 62.66 | 14.30 | 16.70 |
| -5 | 65.73 | 7.78 | 6.95 |
| 0 | 64.36 | 1.64 | -6.61 |
| 5 | 68.22 | -10.67 | -21.23 |
| 10 | 68.08 | -16.63 | -30.43 |
| 15 | 66.55 | -22.01 | -42.25 |
| 20 | 68.08 | -18.76 | -52.73 |
| 25 | 72.55 | 3.82 | -63.47 |
| 30 | 79.21 | 12.15 | -48.38 |
| 35 | 80.38 | 14.82 | -37.46 |
| 40 | 80.72 | 15.13 | -24.81 |
| 45 | 81.07 | 13.92 | -20.94 |
| 50 | 77.08 | -14.16 | -21.65 |
| 55 | 71.08 | -9.17 | -8.40 |
| 60 | 68.90 | -8.82 | 0.60 |
| 65 | 63.44 | -8.03 | 14.95 |
| 70 | 62.46 | 10.61 | 35.50 |
| 75 | 62.27 | 11.39 | 38.31 |
| 80 | 59.78 | 13.77 | 35.07 |
| 85 | 59.52 | 8.70 | 23.97 |
| 90 | 59.95 | 4.26 | 10.51 |

**Table 11b. Unsteady Flow CFD Results vs. Angle of Attack, Refined Grid**

| Angle of Attack deg | Drag ft$^2$ | Lift ft$^2$ | Pitch Moment ft$^3$ |
|---|---|---|---|
| | $C_DA$ | $C_LA$ | $C_mAL$ |
| -45 | 72.12 | 1.43 | 5.08 |
| -40 | 71.85 | -0.68 | 10.08 |
| -35 | 69.75 | 1.37 | 15.41 |
| -30 | 68.66 | 4.30 | 22.30 |
| -25 | 66.69 | 7.29 | 32.36 |
| -20 | 64.59 | 11.73 | 38.63 |
| -15 | 61.67 | 10.48 | 41.66 |
| -10 | 59.71 | 10.48 | 35.00 |
| -5 | 57.98 | 6.72 | 20.30 |
| 0 | 59.86 | 2.28 | 2.33 |
| 5 | 59.27 | 10.23 | -15.91 |
| 10 | 58.40 | -12.16 | -30.16 |
| 15 | 60.14 | -11.34 | -37.52 |
| 20 | 62.51 | -7.69 | -37.65 |
| 25 | 66.23 | -2.67 | -31.82 |
| 30 | 67.27 | 0.31 | -23.03 |
| 35 | 69.47 | -3.91 | -16.66 |
| 40 | 69.63 | 2.45 | -9.47 |
| 45 | 70.55 | -5.54 | -6.68 |

# APPENDIX F    UNSTEADY DATA, REPEAT AT ZERO PITCH, ZERO SIDESLIP

### Table 12.  Unsteady Flow CFD Results - DES-SA Turbulence Model – Repeat Runs for Repeatability, Grid with Skids

| Run # | Force Coefficients ft$^2$ | | Pitching moment ft$^3$ |
|---|---|---|---|
| | $C_DA$ | $C_LA$ | $C_mAL$ |
| 1 | 61.91 | 3.33 | -12.91 |
| 2 | 64.95 | 2.89 | -5.68 |
| 3 | 65.64 | 2.33 | -2.56 |
| 4 | 64.73 | 3.28 | -5.56 |
| 5 | 63.11 | 0.47 | -7.72 |
| 6 | 65.38 | -1.88 | -6.62 |
| 7 | 62.32 | 1.55 | -5.79 |
| 8 | 66.80 | 1.15 | -6.05 |
| Average | 64.36 | 1.64 | -6.61 |
| min | 61.91 | -1.88 | -12.91 |
| max | 68.80 | 3.33 | -2.56 |
| stdv | 1.73 | 1.76 | 2.93 |

## APPENDIX G    WIND TUNNEL DATA FOR STATIONARY CONEX

### Table 13: Wind Tunnel Data: Static Aerodynamics vs. Side Slip Angle at $\alpha = 0$

| Sideslip angle deg | yaw $C_nAL$ ft³ | pitch $C_mAL$ ft³ | Roll $C_lAL$ ft³ | lift $C_LA$ ft² | drag $C_DA$ ft² | side $C_YA$ ft² |
|---|---|---|---|---|---|---|
| 0 | 0 | -23.78 | 0 | 0.82 | 62.92 | 0 |
| 5 | 13.68 | -17.97 | -0.13 | 7.74 | 61.13 | 11.48 |
| 10 | 28.27 | -12.75 | -0.56 | 12.28 | 59.13 | 18.03 |
| 15 | 32.95 | -14.98 | -2.66 | 11.02 | 59.72 | 17.36 |
| 20 | 33.48 | -15.35 | -6.11 | 9.07 | 60.77 | 16.00 |
| 25 | 29.66 | -18.83 | -12.72 | 5.60 | 62.07 | 15.29 |
| 30 | 24.35 | -20.06 | -18.67 | 3.78 | 63.64 | 15.72 |
| 35 | 21.95 | -21.39 | -22.52 | 4.00 | 64.80 | 16.55 |
| 40 | 18.20 | -29.00 | -25.68 | 2.89 | 65.24 | 17.21 |
| 45 | 13.25 | -33.78 | -25.91 | 3.05 | 65.00 | 16.97 |
| 50 | 8.13 | -30.23 | -22.88 | 2.08 | 62.49 | 13.61 |
| 55 | -2.52 | -26.11 | -17.80 | -1.20 | 59.32 | 5.35 |
| 60 | -12.29 | -25.04 | -12.32 | -3.63 | 56.73 | 1.82 |
| 65 | -22.98 | -18.33 | -8.70 | -3.00 | 53.18 | 0.97 |
| 70 | -35.57 | -12.42 | -5.08 | -1.62 | 48.61 | 0.22 |
| 75 | -45.84 | -7.24 | -2.26 | -1.05 | 45.19 | -2.84 |
| 80 | -46.07 | -9.00 | 1.30 | -1.09 | 42.58 | -6.19 |
| 85 | -23.32 | -5.38 | 2.13 | -0.90 | 42.28 | -6.19 |
| 90 | 0 | -0.36 | 0 | -0.36 | 42.82 | 0 |

**Table 14: Wind Tunnel Data: Static Aerodynamics vs. Angle of Attack at β = 0**

| Angle of Attack deg | Forces ft² | | Pitching Moment ft³ |
| --- | --- | --- | --- |
| | $C_DA$ | $C_LA$ | $C_mAL$ |
| -90 | 48.33 | 0 | 0 |
| -85 | 50.83 | -13.37 | -26.87 |
| -80 | 54.17 | -13.39 | -32.72 |
| -75 | 57.85 | -10.36 | -37.60 |
| -70 | 62.45 | -8.78 | -36.10 |
| -65 | 66.58 | -6.29 | -32.58 |
| -60 | 69.82 | -3.12 | -27.14 |
| -55 | 72.92 | -2.19 | -21.56 |
| -50 | 74.55 | 3.58 | -18.67 |
| -45 | 76.02 | 3.67 | -13.75 |
| -40 | 75.64 | 6.26 | -8.27 |
| -35 | 76.02 | 10.08 | -6.44 |
| -30 | 74.86 | 10.85 | -0.50 |
| -25 | 72.16 | 11.99 | 3.55 |
| -20 | 68.86 | 13.22 | 7.57 |
| -15 | 64.59 | 14.79 | 10.53 |
| -10 | 61.22 | 16.89 | 6.64 |
| -5 | 59.20 | 17.13 | 2.39 |
| 0 | 62.92 | 0.82 | -23.78 |
| 5 | 64.43 | -9.52 | -34.94 |
| 10 | 64.70 | -17.88 | -48.23 |
| 15 | 66.15 | -18.90 | -60.58 |
| 20 | 68.47 | -11.75 | -71.35 |
| 25 | 72.61 | -5.54 | -69.82 |
| 30 | 75.98 | -1.19 | -60.19 |
| 35 | 78.84 | 1.00 | -47.26 |
| 40 | 80.75 | -1.58 | -38.30 |
| 45 | 80.24 | 2.64 | -25.71 |
| 50 | 79.00 | 4.10 | -16.67 |
| 55 | 76.56 | 10.91 | -5.78 |
| 60 | 73.71 | 11.57 | 2.26 |
| 65 | 70.91 | 12.62 | 19.93 |
| 70 | 69.08 | 14.12 | 34.14 |
| 75 | 65.78 | 16.08 | 43.47 |
| 80 | 66.23 | 20.70 | 33.88 |
| 85 | 65.99 | 12.17 | 18.37 |
| 90 | 66.76 | 0 | 0 |

## APPENDIX H:  FLOW FIELD FIGURES FOR VARIOUS SIDE SLIP ANGLES, VIEW FROM ABOVE +Z

The following sequence of snapshots depicting the flow field about the CONEX as a function of side slip angle. The view is from the  +Z axis.
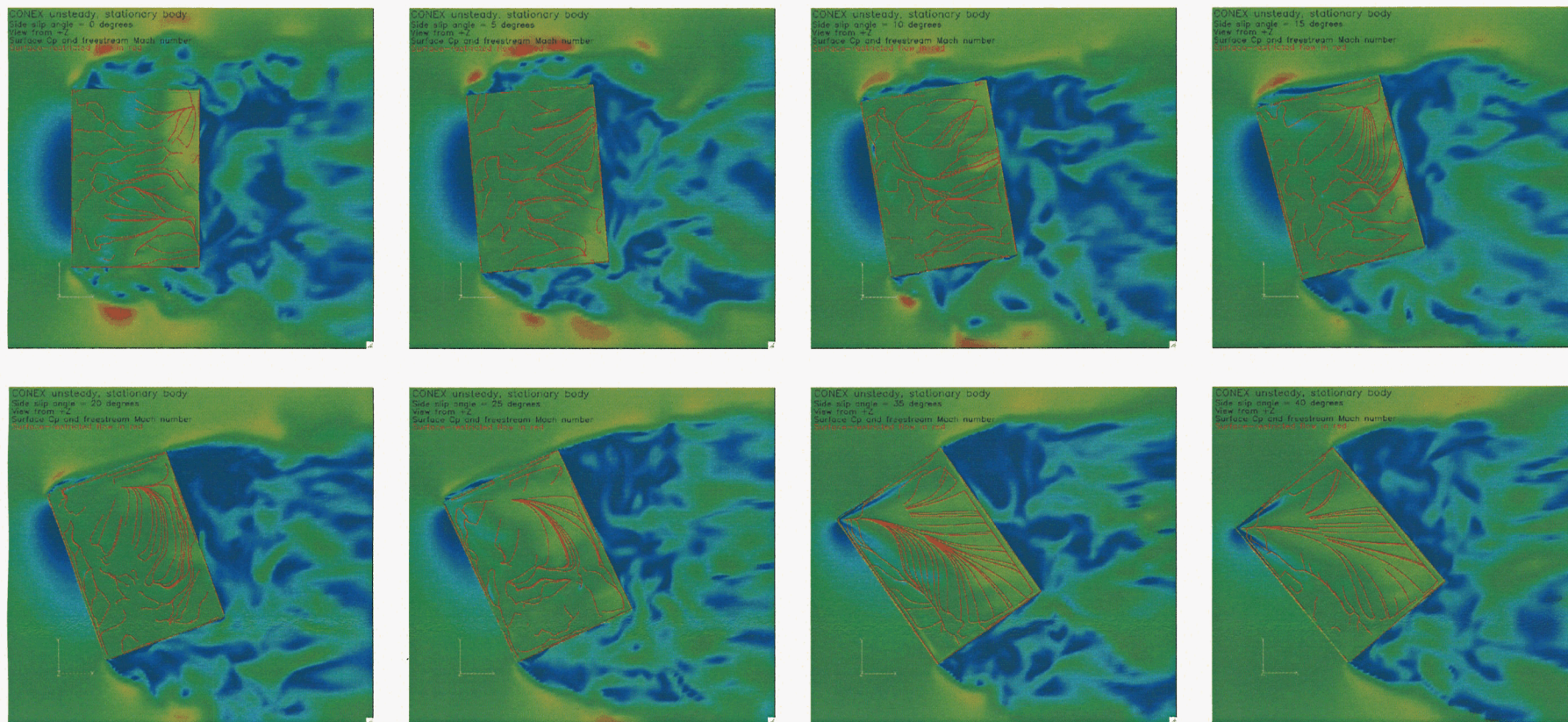
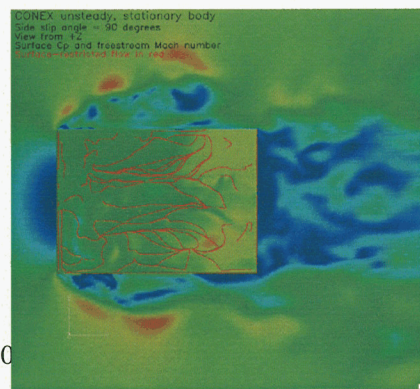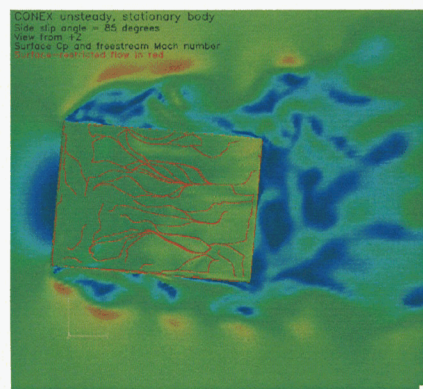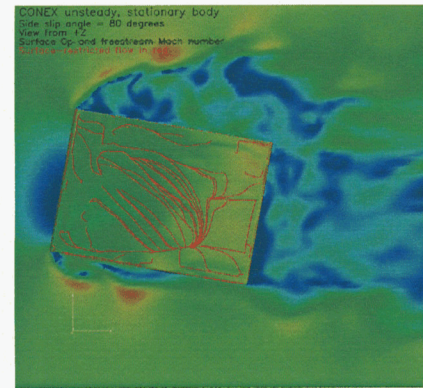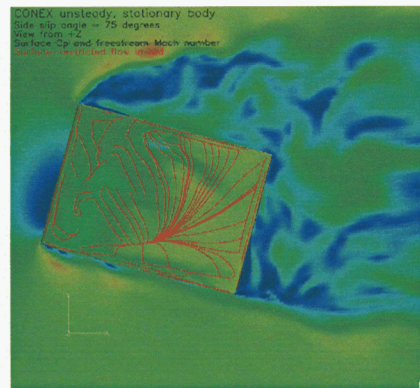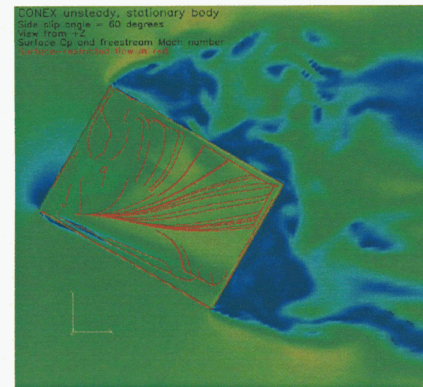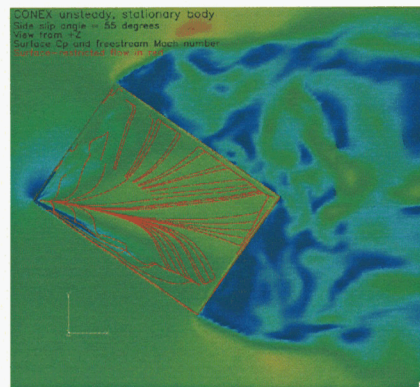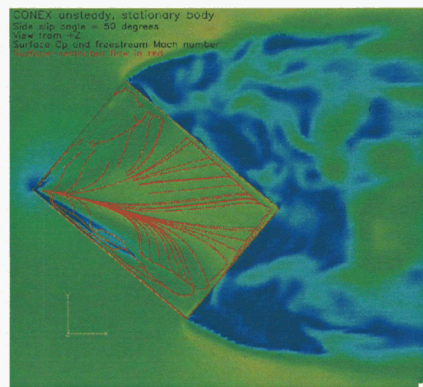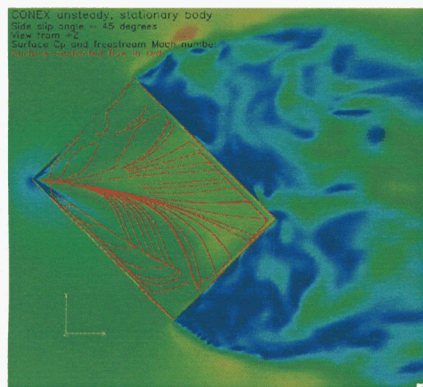*Figure 31. Flow Field Figures as a Function of Side Slip Angle, View +Z*
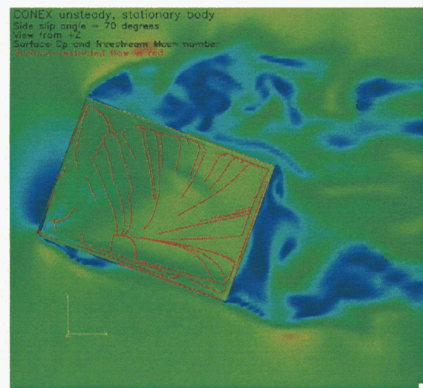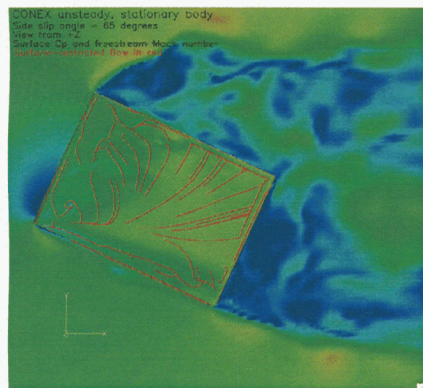
*Figure 31. (Continued) Flow Field Figures as a Function of Side Slip Angle, View +Z*

## APPENDIX I: FLOW FIELD FIGURES FOR VARIOUS SIDE SLIP ANGLES, VIEW FROM -Y

The following sequence of snapshots depicting the flow field about the CONEX as a function of side slip angle. The view is from the −Y axis.
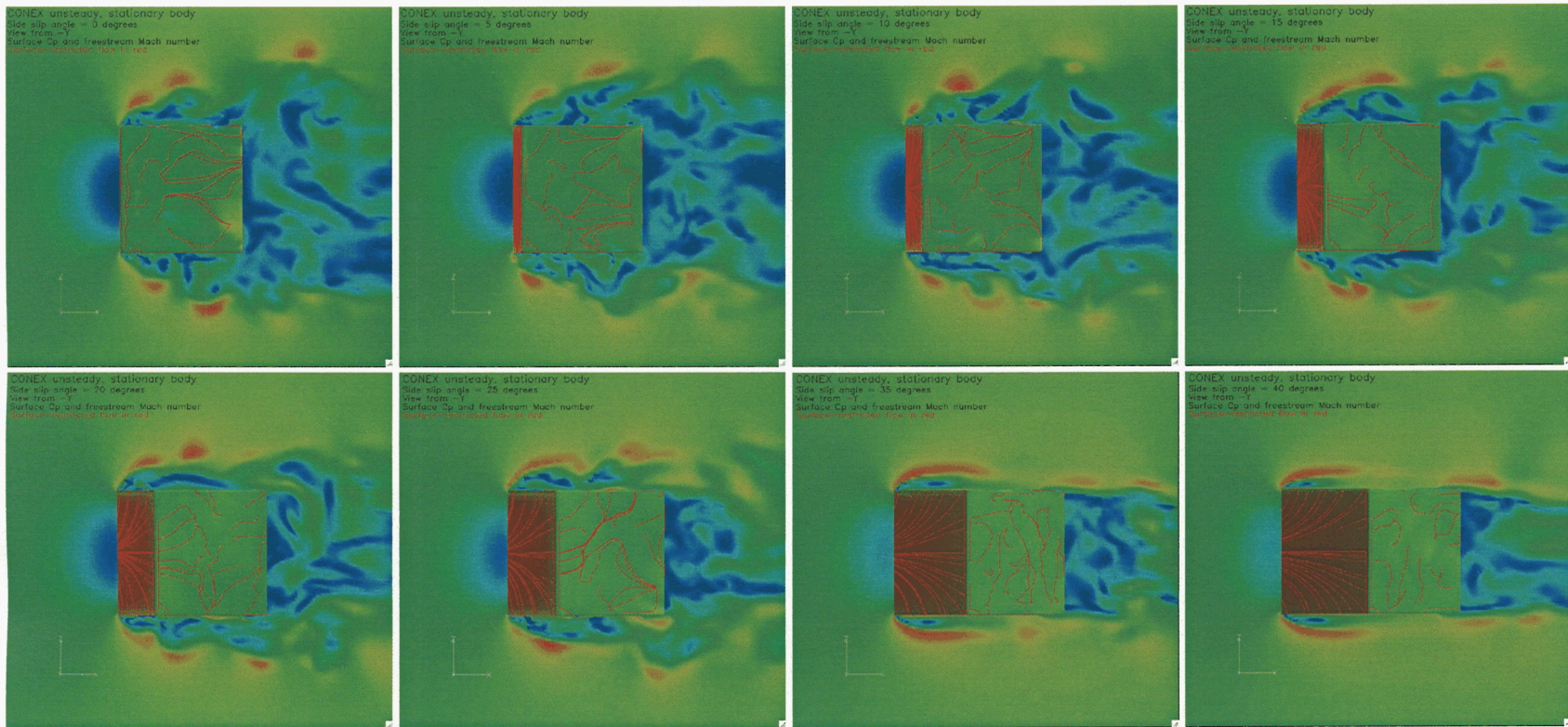
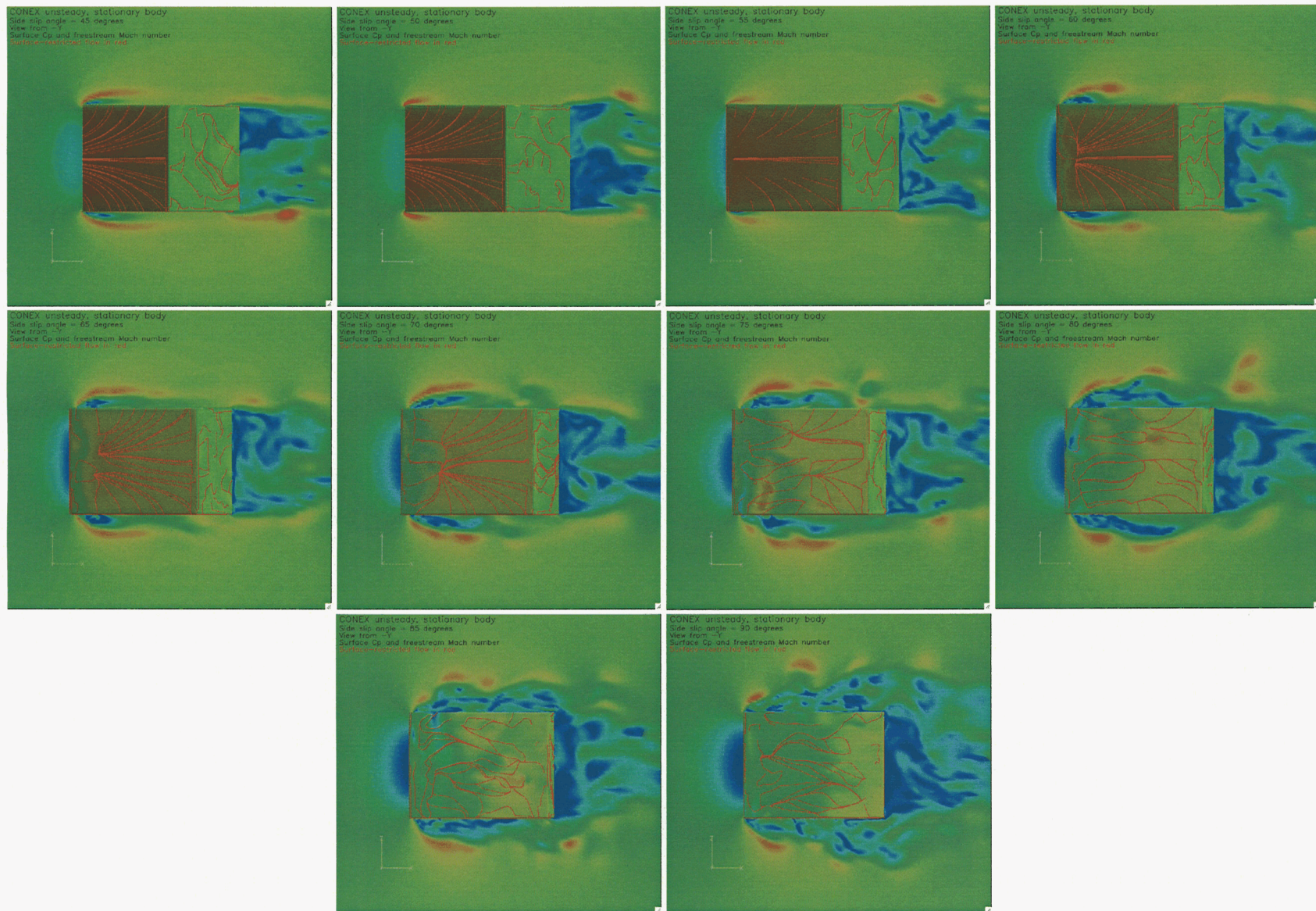*Figure 32. Flow Field Figures as a Function of Side Slip Angle, View -Y*

*Figure 32. (Continued) Flow Field Figures as a Function of Side Slip Angle, View -Y*

# INITIAL DISTRIBUTION LIST

| | | Copies |
|---|---|---|
| | | Electronic |

Weapon Systems Technology Information
Analysis Center
1901 N. Beauregard Street, Suite 400
Alexandria, VA 22311-1720

Ms. Vakare Valaitis
vvalaitis@alionscience.com — Electronic

Defense Technical Information Center
8725 John J. Kingman Rd., Suite 0944
Fort Belvoir, VA 22060-6218

Jack Rike
jrike@dtic.mil — Electronic

Department of Mechanical Engineering
Northern Arizona University
Dr. Earl P. N. Duque        earl.duque@nau.edu — Electronic
Dr. Johannes Theron        jantheron@hotmail.com — Electronic
Flagstaff, AZ 86011

Faculty of Aerospace Engineering
Technion Israel Institute of Technology
Dr. Aviv Rosen        rosen@aerodyne.technion.ac.il — Electronic
Dr. Rachel Gordon        rgordon@techunix.technion.ac.il — Electronic
Haifa 32000, Isreal

AMSRD-AMR — Electronic

AMSRD-AMR-AF,        Mr. Chris Blanken — Electronic
                          cblanken@mail.arc.nasa.gov
                          Mr. Luigi Cicolani — Electronic
                          lcicolani@mail.arc.nasa.gov
                          Dr. Thomas Maier — Electronic
                          tmaier@mail.arc.nasa.gov
                          Dr. Mark Tischler — Electronic
                          mtischler@mail.arc.nasa.gov

AMSRD-AMR-CS-IC — Electronic

AMSRD-L-G-I,        Ms. Anne Lanteigne — Electronic
                          anne.lanteigne@us.army.mil